Incorporating Full Elastodynamic Effects and Dipping Fault Geometries in Community Code Verification Exercises for Simulations of Earthquake Sequences and Aseismic Slip (SEAS)

Brittany A. Erickson* et al.

ABSTRACT -

Numerical modeling of earthquake dynamics and derived insight for seismic hazard relies on credible, reproducible model results. The sequences of earthquakes and aseismic slip (SEAS) initiative has set out to facilitate community code comparisons, and verify and advance the next generation of physics-based earthquake models that reproduce all phases of the seismic cycle. With the goal of advancing SEAS models to robustly incorporate physical and geometrical complexities, here we present code comparison results from two new benchmark problems: BP1-FD considers full elastodynamic effects, and BP3-QD considers dipping fault geometries. Seven and eight modeling groups participated in BP1-FD and BP3-QD, respectively, allowing us to explore these physical ingredients across multiple codes and better understand associated numerical considerations. With new comparison metrics, we find that numerical resolution and computational domain size are critical parameters to obtain matching results. Codes for BP1-FD implement different criteria for switching between quasi-static and dynamic solvers, which require tuning to obtain matching results. In BP3-QD, proper remote boundary conditions consistent with specified rigid body translation are required to obtain matching surface displacements. With these numerical and mathematical issues resolved, we obtain excellent quantitative agreements among codes in earthquake interevent times, event moments, and coseismic slip, with reasonable agreements made in peak slip rates and rupture arrival time. We find that including full inertial effects generates events with larger slip rates and rupture speeds compared to the quasi-dynamic counterpart. For BP3-QD, both dip angle and sense of motion (thrust versus normal faulting) alter ground motion on the hanging and foot walls, and influence event patterns, with some sequences exhibiting similar-size characteristic earthquakes, and others exhibiting different-size events. These findings underscore the importance of considering full elastodynamics and nonvertical dip angles in SEAS models, as both influence short- and long-term earthquake behavior and are relevant to seismic hazard.

KEY POINTS

- We develop new quantitative metrics for comparing both long-term and short-term features of SEAS simulations.
- We obtain quantitative agreements among simulations incorporating elastodynamic effects and dipping faults.
- Full dynamics and nonvertical dip angles are important in SEAS models and can inform seismic hazard.

Supplemental Material

INTRODUCTION

Improving our understanding of earthquake processes is essential for minimizing their devastating effects on society and the human environment. Natural fault zones can remain stuck for century- to millennial-long periods until undergoing bursts of rapid rupture during large earthquakes, and it is not well known what governs the recurrence intervals and magnitudes of large events and the associated ground motion. One of the main goals in earthquake science is the development of robust, predictive

Full author list and affiliations appear at the end of this article.

*Corresponding author: bae@uoregon.edu

Cite this article as Erickson, B. A., J. Jiang, V. Lambert, S. D. Barbot, M. Abdelmeguid, M. Almguist, J.-P. Ampuero, R. Ando, C. Cattania, A. Chen, et al. (2023). Incorporating Full Elastodynamic Effects and Dipping Fault Geometries in Community Code Verification Exercises for Simulations of Earthquake Sequences and Aseismic Slip (SEAS), Bull. Seismol. Soc. Am. 113, 499-523, doi: 10.1785/ 0120220066

© Seismological Society of America

earthquake models that shed light on what is physically possible and plausible, given the inherently limited observations of the Earth. Therefore, an important component of this endeavor is the inclusion of realistic physics and geometries, while developing computationally tractable simulations. A spectrum of modeling environments have emerged within the scientific community, with different focuses on the multiscale features in space- and time-characterizing earthquake source processes.

At one end of the spectrum of earthquake modeling are the single-event dynamic rupture simulations, which have been extensively used to explore earthquake behavior and rupture propagation. Advanced numerical methods have incorporated a variety of geometric and physical complexities such as non-planar faults and off-fault plasticity (e.g., Harris and Day, 1993; Dunham et al., 2011; Shi and Day, 2013). However, single-event dynamic rupture simulations are generally limited to the time scales of wave propagation (seconds to minutes), in which challenges arise in how to choose appropriate initial conditions (such as proper nucleation procedures under the heterogeneous stress conditions) consistent with loading and prior fault slip history over decadal-to-centennial time scales.

At the other end of the modeling spectrum are earthquake simulators that were developed to model earthquake sequences on millennial time scales in large-scale, complex fault networks (Richards-Dinger and Dieterich, 2012; Tullis *et al.*, 2012a). To make such large-scale simulations computationally tractable, earthquake simulators rely on simplifying assumptions for fault loading conditions, treatments of fault friction, approximations of seismic wave effects, are limited to the linear elastic bulk material response and require the use of large computational cells (Rundle *et al.*, 2006; Dieterich and Richards-Dinger, 2010; Ward, 2012). The missing physical effects, such as aseismic slip, wavemediated dynamic stress transfers, and inelastic bulk response could potentially dominate earthquake and fault interactions.

A complementary modeling framework to those offered by the dynamic rupture simulations and earthquake simulators are simulations of sequences of earthquakes and aseismic slip (SEAS; Erickson et al., 2020; Jiang et al., 2022; and references therein). SEAS models focus on smaller, regional-scale fault zones and aim to understand what physical factors control the full range of observations of aseismic slip, nucleation locations and the earthquakes themselves (dynamic rupture events), ground shaking, damage zone evolution, afterslip and aftershocks, magnitudes, and recurrence intervals of large earthquakes (e.g., Kaneko et al., 2011; Barbot et al., 2012; Lambert and Barbot, 2016; Jiang and Lapusta, 2017; Abdelmeguid et al., 2019; Cattania, 2019; Harvey et al., 2022). Such SEAS models can inform the initial conditions and nucleation procedures for dynamic rupture simulations, and identify important physical ingredients, as well as appropriate approximations, that could be included in larger scale, longer term earthquake simulators.

Earlier methods for SEAS simulations made simplifying assumptions to ease computations, including a linear elastic

material response, approximate elastodynamic effects, simple fault geometries (e.g., single planar faults or small fault networks), and/or 2D scenarios (e.g., Tse and Rice, 1986; Rice, 1993). However, recent advancement of SEAS computational methods have enabled simulations with additional physical and/or geometrical features, including full inertial effects, material and frictional heterogeneities, and nonplanar fault geometries in 3D volumes (e.g., Lapusta and Rice, 2003; Kaneko et al., 2011; Ariyoshi et al., 2012; Erickson and Dunham, 2014; Erickson et al., 2017; Allison and Dunham, 2018; Preuss et al., 2019; Dunyu et al., 2020; Barbot, 2021; Dal Zilio et al., 2021; Romanet and Ozawa, 2021; Shi et al., 2022). The inclusion of full inertia (as opposed to the radiation damping approximation of Rice, 1993) generates dynamic stress transfers that tend to increase slip rates and rupture speeds (e.g., Lapusta et al., 2000), and can generate qualitatively different event dynamics, including pulse-like ruptures (Thomas et al., 2014), the transition to supershear (e.g., Andrews, 1976a; Harris and Day, 1993), and the probability that ruptures jump between different fault segments (Lambert and Lapusta, 2021). On the other hand, geometric complexities (for example fault nonplanarity and nonvertical dipping faults) can significantly alter the resulting ground motion in terms of high-frequency content and asymmetry of shaking across the fault trace, which have direct implications for seismic hazard assessment (e.g., Duan and Oglesby, 2005; Ma and Beroza, 2008).

As SEAS models are being used to explain, reproduce, and predict earthquake behavior in more physically and geometrically complex settings, the critical step remains to ensure that these methodologies are accurate. The dynamic rupture simulations and the earthquake simulators have undergone extensive testing, comparing results from different codes developed to address the computational challenges associated with the particular temporal and spatial scales under consideration (Harris et al., 2009, 2018; Tullis et al., 2012b; Barall and Harris, 2014). The advancement of SEAS models also requires rigorous testing to verify outcomes over scales specific to SEAS problems: temporal resolution of the pre-, inter-, and postseismic periods as well as spontaneous earthquake nucleation, and the spatial resolution of physical processes relevant to dynamic wave propagation and longer term features such as interseismic healing of the fault zone, viscoelasticity, and fluid flow.

Our first two benchmark problems BP1-QD and BP2-QD constitute the very first SEAS code verification exercises (Erickson *et al.*, 2020), in which "-QD" means quasi-dynamic approximation. Although relatively simple in setup (e.g., 2D antiplane problem, with a vertically embedded, planar fault), these benchmarks were designed to test the capabilities of different computational methods in correctly solving a mathematically well-defined, basic problem in crustal faulting. Our follow-up benchmark problems addressed important issues in 3D SEAS simulations, in particular, exploring how various numerical and physical factors affect complex observables at often marginal numerical resolutions (Jiang *et al.*, 2022). The successes of these

TABLE 1

BP1-FD: Details of Participating Simulations of Earthquake Sequences and Aseismic Slip (SEAS) Codes and Modeling Groups

Code Name	Туре	Simulation (Group Members)*	References		
FEBE GARNET	Hybrid FEM/SBEM FDM	abdelmeguid (Abdelmeguid and Elbanna) li (M. Li, Dal Zilio, Pranger, and van Dinther)	Hajarolasvadi and Elbanna (2017), Abdelmeguid <i>et al.</i> (2019) Pranger (2020), Li <i>et al.</i> (2022), https://bitbucket.org/cpranger/garnet/ (last accessed December 2022)		
sem2dpack	SEM	liang (Liang and Ampuero)	https://github.com/jpampuero/sem2dpack (last accessed December 2022)		
Thrase	FDM	harvey (Harvey, Chen, Kozdon, and Erickson)	Kozdon et al. (2020), Erickson et al. (2022), https://github.com/Thrase/Thrase (last accessed December 2022)		
BICyclE	SBEM	jiang (Jiang) lambert (Lambert and Lapusta)	Lapusta et al. (2000), Lapusta and Liu (2009)		
SPEAR	SEM	thakur (Thakur, Huang, and Kaneko)	https://github.com/thehalfspace/Spear (last accessed December 2022)		

^{*}The names of simulations displayed on our online platform. FDM, Finite difference method; FEM, finite-element method; SBEM, spectral boundary element method; and SEM, spectral element method.

TABLE 2 **BP3-QD: Details of Participating SEAS Codes and Modeling Groups**

Code Name	Туре	Simulation (Group Members)*	References
Sbplib	FDM	almquist (Almquist and Dunham)	doi: 10.1016/j.jcp.2020.109842 and 1 https://sourceforge.net/projects/elastic-package-test/ (last accessed December 2022)
Unicycle	BEM	barbot (Barbot)	Barbot (2019), https://bitbucket.org/sbarbot (last accessed December 2022)
FDRA	BEM	cattania (Cattania, Sun, and Segall)	Segall and Bradley (2012), Bradley (2014)
TriBIE	BEM	dli (D. Li, Perez-Silva, and Gabriel)	Li and Liu (2016, 2017), https://github.com/daisy20170101/TriBIE (last accessed December 2022)
FDCycle	FDM	erickson (Erickson)	Erickson and Dunham (2014), https://github.com/brittany-erickson/FDCycle (last accessed December 2022)
ESAM	BEM	liu (Y. Liu)	Liu and Rice (2007)
HBI	BEM	ozawa (Ozawa and Ando)	Ozawa and Ando (2021), https://github.com/sozawa94/hbi (last accessed December 2022)
tandem	DGFEM	uphoff (Uphoff and Gabriel)	https://github.com/TEAR-ERC/tandem (last accessed December 2022)

^{*}The names of simulations displayed on our online platform. BEM, Boundary element method; and DGFEM, discontinuous-Galerkin finite-element method.

exercises have encouraged the SEAS group to consider problems with increased physical and geometric complexities.

In this article, we present results from two new benchmarks, BP1-FD and BP3-QD. Benchmark BP1-FD, with "-FD" indicating a fully dynamic problem, is our first benchmark problem in which we consider fully dynamic earthquake rupture and seismic wave propagation, constituting an important step toward incorporating inertial effects into SEAS models. BP3-QD is the first SEAS benchmark considering a 2D plane-strain problem, in which a dipping fault intersects the free surface and induces changes in normal stress on the fault. In this work, our goal is twofold: to showcase agreements made across participating codes in the two benchmark problems and to highlight some of the differences that these added features have on SEAS model outcomes.

We organize the article as follows: first, we provide details of the SEAS working group, including information on participating modeling groups and codes. Then we provide an overview of the SEAS strategy for benchmark design, and detail the mathematical problem statements for both BP1-FD and BP3-QD. We share results from participating modeling groups, with quantitative comparisons made through specifically defined metrics, along with a discussion of model outcomes influenced by the new physics and geometries considered. The final section provides a summary of findings.

SEAS COORDINATION AND MODELING GROUPS

The overall goal of the SEAS working group has been to verify SEAS models that address important problems in earthquake science, while maximizing participation within the scientific community. These exercises involve the comparison of different computational methods to assess our capacity to accurately resolve detailed fault-slip history over a range of time scales. These efforts have required us to better understand the dependence of fault slip history on initial conditions, model spin-up, fault properties, and friction laws.

A total of seven and eight modeling groups participated in BP1-FD and BP3-QD, respectively. Details of the codes and

modeling groups are provided in Tables 1 and 2, along with a summary of computational methods, including spectral boundary element/boundary element (SBEM/BEM), finite difference, and discontinuous-Galerkin/spectral/finite element (DGFEM/SEM/FEM) methods. The two modeling groups independently perform simulations using the same code BICyclE for BP1-FD (hereinafter, jiang, denoted as BICyclE-1 and lambert, denoted as BICyclE-2).

Our benchmark descriptions constitute a mathematically well-defined problem; however, all modeling groups must formulate it to suit their particular numerical framework. For example, the quasi-dynamic assumption made in BP3-QD means that the problem can be formulated as either an ordinary differential equation (ODE) system or an index-1 differential algebraic equation (DAE). BP1-FD, on the other hand, naturally gives rise to an ODE system; however, some codes assume that inertia is negligible during the interseismic phases (e.g., by codes utilizing a switching method); thus, the problem can be formulated similarly to BP3-QD during the aseismic phases. Particular choices of the problem formulation differ among the groups; details for each code can be found in the associated references listed in Tables 1 and 2. In addition (and as will be described in the Benchmark descriptions section), the benchmark problems consider semi-infinite spatial domains. Some numerical schemes must make choices for finite domain sizes and boundary conditions that effectively represent these semi-infinite domains. Details differentiating individual codes and specific choices for these parameters are discussed when relevant.

In addition to problem formulations and domain considerations, all SEAS codes must adopt a method for time stepping. For both benchmark problems, all groups apply either the adaptive time-stepping method of Lapusta *et al.* (2000) or some variant of a high-order accurate Runge–Kutta (RK) method, or both. Although specific details can be found in the references listed in Tables 1 and 2, we discuss a few details here to highlight choices made by participating groups.

For BP3-QD, all codes adopt a high-order accurate (either 2/3 or 4/5), adaptive, and explicit RK method. For BP1-FD, the pure SBEM code (BICyclE) utilizes the method of Lapusta *et al.* (2000) throughout the simulation; some other codes (sem2d-pack, SPEAR, FEBE) do so during the interseismic phases but switch to an explicit RK method during the coseismic phases (details of such a switch between solvers is further discussed in the section BP1-FD model comparisons). The volume-based code Thrase utilizes both adaptive and constant-step size RK methods for the interseismic/coseismic regimes, respectively, whereas the volume-based code GARNET integrates implicitly through the whole simulation period (i.e., no switch between solvers is needed) with time stepping done according to Lapusta *et al.* (2000).

In this study, we do not directly compare the sensitivity of modeling results to choices in time-stepping procedures among modeling groups. Although the numerical time integration scheme and choices in associated error tolerance may affect the timing of earthquakes (e.g., appendix D in Dublanchet, 2022), each adaptive time-stepping method can be tuned through a number of internal parameters specific to the methodology, and we left this to participating groups to individually explore appropriate values. Although time stepping can contribute, in part, to observed discrepancies among simulated results, we find that the results for the considered benchmark problems are quite sensitive to numerical factors like model domain size and cell size, and focus on these features in the current work.

In this study, we compare model outcomes across codes by both visual inspection and quantitative assessment. We use the phrase "good agreements" to mean that results across modeling groups look similar upon visual inspection. We deem particular problem formulations and/or numerical parameters (e.g., computational domain size) "sufficient", meaning that model outcomes are in good agreement with these particular choices. We reserve the term "excellent agreement" when referring to a quantitative measure of error being within a few percent of a well-resolved reference solution.

BENCHMARK DESCRIPTIONS

Here, we include specific details of the mathematical problem statements for BP1-FD and BP3-QD, including friction, coordinate system, and loading conditions (along with a description of relevant parameters) to aid the analysis and discussion of results.

In both benchmark problems, we assume that a planar fault is embedded in a homogeneous, linear elastic half-space defined by

$$(x,y,z) \in (-\infty,\infty) \times (-\infty,\infty) \times (0,\infty), \tag{1}$$

with a free surface at z=0 and z as positive downward, see Figure 1. We assume either antiplane shear (BP1-FD) or plane strain motion (BP3-QD), effectively reducing both problems to two dimensions. In the upper section of the fault (i.e., from the surface to a down-dip distance of W_f), we equate shear stress τ with fault shear resistance, namely

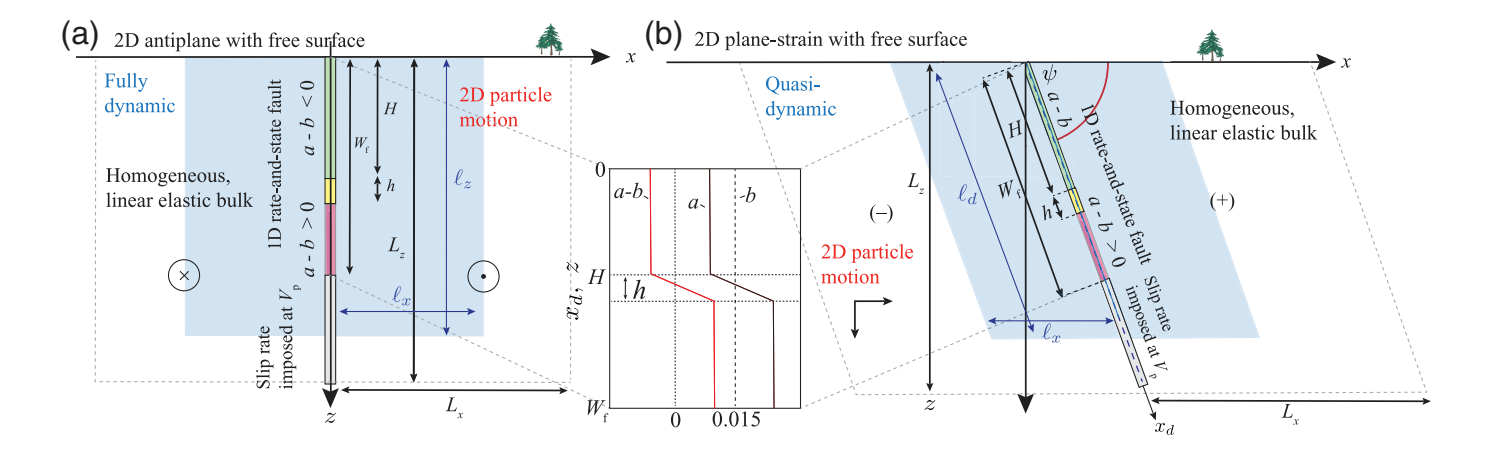
$$\tau = F(V, \theta, \bar{\sigma}_n), \tag{2}$$

in which τ and slip rate V are scalar valued for these 2D problems. We consider rate-and-state friction in which $F = \bar{\sigma}_n f(|V|, \theta) \frac{V}{|V|}$, in which θ is the state variable (Dieterich, 1979; Ruina, 1983; Marone, 1998). The effective normal stress:

$$\bar{\sigma}_n = (\sigma^0 - p^0) + \Delta \sigma, \tag{3}$$

takes into account possible changes in normal stress $\Delta \sigma$ induced by slip on the fault, in which $\bar{\sigma}_n^0 = (\sigma^0 - p^0)$ is the initial effective normal stress, and changes in pore-fluid pressure p are neglected. We assume that normal stress is positive in compression. θ evolves according to the aging law (Ruina, 1983):

$$\frac{d\theta}{dt} = 1 - \frac{|V|\theta}{D_{RS}},\tag{4}$$



in which $D_{\rm RS}$ (sometimes denoted L or D_c in rate-and-state studies) is the characteristic slip distance. As done in Jiang *et al.* (2022), we opt to use this notation to avoid confusion with the critical slip distances " D_c " and " d_c " of linear slip-weakening friction and seismic estimates, and to distinguish from spatial scales (like computational domain size) that use "L". The friction coefficient f is given by a regularized formulation (Lapusta *et al.*, 2000):

$$f(V,\theta) = a \sin h^{-1} \left[\frac{V}{2V_0} \exp\left(\frac{f_0 + b \ln(V_0 \theta/D_{RS})}{a}\right) \right], \quad (5)$$

in which f_0 is a reference friction coefficient for reference slip rate V_0 . Depth-dependent frictional parameters a and b define a shallow seismogenic region with velocity-weakening (VW) friction and a deeper velocity-strengthening (VS) region, below which a relative plate motion rate $V_{\rm p}$ is imposed.

Parameters of important relevance for results in all of our benchmark problems to date include the process zone Λ , which describes the spatial region near the rupture front under which breakdown of fault resistance occurs (Palmer and Rice, 1973). For fully dynamic rupture simulations, the size of the process zone decreases with increasing rupture speed and shrinks toward zero as the rupture speed approaches the limiting wavespeed (Rayleigh wavespeed for plane strain problems and shear wavespeed for antiplane problems, e.g., Day *et al.*, 2005). For fault models governed by rate-and-state friction, the quasistatic process zone at a rupture speed of 0^+ , Λ_0 , can be estimated (Day *et al.*, 2005; Ampuero and Rubin, 2008; Perfettini and Ampuero, 2008) as

$$\Lambda_0 = C \frac{\mu^* D_{\rm RS}}{b \bar{\sigma}_n^0},\tag{6}$$

in which *C* is a constant of order 1, and μ^* is the effective stiffness of the surrounding material ($\mu^* = \mu$ for antiplane strain and $\mu^* = \mu/(1 - \nu)$ for plane strain, in which ν is Poisson's ratio).

Another characteristic length scale that has been shown to control model behavior is the critical nucleation size h^* , which

Figure 1. Both benchmark problems (a) BP1-FD and (b) BP3-QD assume a planar fault embedded in a homogeneous, linear elastic half-space with a free surface. The fault is governed by rate-and-state friction to a distance down-dip W_f and creeps at an imposed constant rate V_p down to the infinite depth. BP1-FD considers antiplane shear, with out-of-plane motion denoted with circles. BP3-QD considers plane strain motion, in which the left and right sides of the fault are labeled with "(–)" and "(+)", respectively. Both benchmarks include the nucleation, propagation, and arrest of earthquakes and aseismic slip in the post- and interseismic periods. The color version of this figure is available only in the electronic edition.

governs the minimum extent of the rate-and-state VW region, in which spontaneous nucleation may occur (Rice and Ruina, 1983; Dieterich, 1992). A related quantity is the critical crack size (Andrews, 1976b,c), the derivation of which assumes slip-weakening friction and the cohesive zone being (much) smaller than the crack size when dynamic slip initiates, which may or may not be true depending on the friction law and loading in the nucleation zone (Uenishi and Rice, 2003; Rubin and Ampuero, 2005; Ampuero and Rubin, 2008; Liu and Lapusta, 2008). For 2D problems with the aging law and 0.5 < a/b < 1, the nucleation size can be well estimated using the critical-crack-size-like considerations as Rubin and Ampuero (2005):

$$h^* = \frac{2}{\pi} \frac{\mu^* b D_{\text{RS}}}{(b-a)^2 \bar{\sigma}_{\text{n}}^0}.$$
 (7)

Throughout this work, we use the term cell size to refer to model resolution, that is, the length between grid points. For numerical methods (such as high-order FEM) that are not based on equally spaced grids, cell size should be interpreted as an average resolution per degree of freedom along the face of an element. In the following sections, we provide information on suggested cell size for each benchmark problem that ensures resolution of length scales in equations (6) and (7).

Computational length scales that have been important in our benchmark problems are those defining the 2D domain: L_x denotes the lateral extent, and L_z denotes the depth extent (see Fig. 1). The problem descriptions consider a semi-infinite

TABLE 3
Parameter Values Used in BP1-FD and BP3-QD

Parameter	Definition	Value Units
ρ	Density	2670 kg/m ³
C_{S}	Shear wavespeed	3.464 km/s
ν	Poisson's ratio	0.25 (BP3-QD only)
$ar{\sigma}_{n}^{0}$	Initial effective normal stress on fault	50 MPa
<i>a</i> ₀	Rate-and-state direct-effect parameter	0.010
a _{max}	Rate-and-state direct-effect parameter	0.025
b_0	Rate-and-state evolution-effect parameter	0.015
D_{RS}	Characteristic state evolution distance	0.008 m
f_0	Reference friction coefficient	0.6
V_0	Reference slip rate	10 ⁻⁶ m/s
$V_{\rm p}$	Plate rate	10 ⁻⁹ m/s (BP1-FD) ±10 ⁻⁹ m/s (BP3-QD)
V_{init}	Initial slip rate	10 ⁻⁹ m/s (BP1-FD) ±10 ⁻⁹ m/s (BP3-QD)
Ψ	Dip angle	30°, 60°, and 90° (BP3- QD only)
Н	Down-dip extent of uniform VW region	15 km
h	Width of VW–VS transition zone	3 km
W_f	Width of rate-and-state fault	40 km
Δz	Suggested cell size	25 m
t_{f}	Final simulation time	1500 yr
L_z	Depth of computational domain	Not specified
L_x	Off-fault distance of computational domain	Not specified

VS, velocity strengthening; and VW, velocity weakening.

half-space, which for many codes means making choices for a representative, finite computational domain size. So, although not specified by the problem description, some codes must make choices for L_z and (for volume-based codes) L_x , along with boundary condition type. In our first benchmark comparison, BP1-QD, we found that the domain needed to be sufficiently large before results showed negligible change upon further domain-size increase (at which point results did not depend on boundary condition type). Perhaps unsurprisingly, this domain-size requirement is also true for BP1-FD and BP3-QD. We report choices of numerical parameters that are critical to model agreement across codes, and mainly show and discuss results for simulations with sufficiently large domains sizes.

All parameters for both the benchmark problems are given in Table 3. Complete details, including initial and boundary/ interface conditions, are included in the supplemental material, available to this article, and on our online platform.

BP1-FD description

BP1-FD is the fully dynamic version of the first benchmark problem BP1-QD (previously referred to as BP1, see Erickson

et al., 2020) and includes the nucleation, propagation (including the generation of seismic waves), and arrest of earthquakes, with aseismic slip in the post- and interseismic periods.

For this benchmark problem, the fault is embedded vertically within a semi-infinite half-space, and we assume 2D antiplane shear motion governed by the momentum balance equation and Hooke's law of linear elasticity, see Figure 1a. The fault intersects the free surface at z=0 and is VW down to a depth H, at which point it transitions to velocity strengthening over a distance h down to a depth W_f . Below W_f , the fault creeps at an imposed constant rate V_p down to infinite depth. The fault shear stress $\tau=\tau^0+\Delta\tau$ involved in equation (2) is the sum of the prestress and the shear stress perturbation (the effects of radiation damping presented in BP1-QD to bound shear stress at seismic slip rates are naturally incorporated in the fully dynamic stress interactions $\Delta\tau$). We let u=u(x,z,t) denote the out-of-plane displacement and assume that right-lateral motion corresponds to positive slip values.

As in BP1-QD, the effective normal stress on the fault is equal to the initial effective normal stress ($\bar{\sigma}_n = \bar{\sigma}_n^0$), as slip on the fault induces no changes in normal stress. We assume the same parameter values as those in BP1-QD, see Erickson *et al.* (2020), except limit the total simulation time to 1500 yr, see Table 3. A suggested cell size of 25 m ensures that Λ_0 and h^* are resolved with 12 and 80 grid points, respectively—the exceptions when such a cell size is not feasible by a participating code.

BP3-QD description

BP3-QD is our first 2D plane strain problem in which a planar fault is embedded in a homogeneous, linear, elastic half-space, dipping at ψ degrees from horizontal, see Figure 1b. The fault intersects the free surface at z = 0; the foot wall $(x \le z \cot \psi)$ and the hanging wall $(x \ge z \cot \psi)$ are designated by (-) and (+), respectively. The down-dip distance is denoted x_d . We let [u, w] = [u(x, z, t), w(x, z, t)] denote the vector of in-plane displacements, with u in the (horizontal) x-direction and w in the (vertical) *z*-direction (with positive values of *w* downward). We assume a quasidynamic response by approximating inertial effects through radiation damping. Rate-and-state friction acts on the fault interface down to $x_d = W_f$, in which shear stress $\tau = \tau^0 + \Delta \tau - \eta V$ is the sum of the prestress, the shear stress change due to quasi-static deformation, and the radiation damping stress. Similar to BP1-FD, the fault is VW down to $x_d = H$, then transitions and is VS down to $x_d = W_f$. Below W_f , the fault creeps at an imposed constant rate V_p .

For our earlier benchmarks BP1-QD and BP2-QD (and including BP1-FD, considered in this work), we only requested fault station time series, which only involve changes in fields across the fault interface. However, these benchmark problems contain an ambiguity in the assumed boundary conditions at infinity, which was revealed in BP3-QD when considering off-fault stations. We resolved this by specifying that stress

changes $\Delta \sigma_{ij}$, and displacement changes (from rigid body translation), $u - u^{\text{rigid}}$ and $w - w^{\text{rigid}}$, vanish at infinity $(x \to \pm \infty, z \to \infty)$. The rigid body translation is given by

$$u^{\pm,\text{rigid}}(t) = \mp \frac{V_{\text{p}}t}{2}\cos\psi, \tag{8a}$$

$$w^{\pm,\text{rigid}}(t) = \mp \frac{V_p t}{2} \sin \psi, \tag{8b}$$

in which both sides of the fault are displaced and reflect the long term, steady-state motion of the fault at depth. For example, for a 90° thrust-fault scenario, the rigid body motion is such that $u^{\pm}=0$, the left side of the fault moves downward $(w^{-}\geq 0)$, and the right side moves up $(w^{+}\leq 0)$; see the complete problem descriptions for more details, including all sign conventions.

Simulations for BP3-QD are compared for three different dip angles of $\psi=30^\circ$, 60° , and 90° and for both thrust- and normal-faulting scenarios. Unlike BP1, the nonvertical dipping fault allows for perturbations from the initial effective normal stress $\bar{\sigma}_n^0$. Our sign conventions are such that thrust faulting has positive values for slip, slip rate, and shear traction; normal faulting has negative values. For the vertical fault case, these fields will be of equal but opposite values for thrust versus normal faulting, therefore, we only share results from the 90° thrust-faulting scenario. For nonvertical faults, however, this symmetry is broken by the fault's intersection with the free surface. A suggested cell-size of 25 m resolves Λ_0 and h^* , with 16 and 100 grid points, respectively—exceptions when such a cell size is not feasible by a participating code.

Computational domain size considerations

Nearly all of the participating codes in BP1-FD and BP3-QD (Tables 1 and 2) are required to make some choices for finite computational domain lengths that sufficiently capture the response of the half-space. The exceptions to this are the BEM-based codes (Unicycle, FDRA, TriBIE, ESAM, and HBI) that only consider the rate-and-state frictional section of the fault, which is discretized down-dip to W_f . Below W_f (and down to infinite depth), steady slip at rate V_p is implicitly imposed through backslip loading.

For the SBEM code (BICyclE), however, the fault is discretized down to a finite depth L_z (below W_f) and subject to periodic boundary conditions, defining a region referred to as a replication cell; in practice, the problem includes an infinite number of fault segments of multiples of L_z . L_z must be sufficiently large so that the interaction among the replicated frictional segments is negligible and approaches the infinite fault case with $L_z \rightarrow \infty$. Backslip is applied by fixing the slip rate V_p at the edges of the replication cell (between L_z and W_f), which introduces a stressing rate on the frictional region consistent with backslip loading at the fixed plate rate. The free-surface

boundary conditions for antiplane motion, as considered in BP1-FD, are induced by introducing a mirror image of the modeled fault domain across the desired free surface (z = 0) in the replication cell when computing the elastic stress transfer (Lapusta *et al.*, 2000). FEBE, which is a hybrid SBEM/FEM code, also chooses L_z in the same manner as BICyclE.

Pure volume-based codes (GARNET, sem2dpack, Thrase, SPEAR, sbplib, FDCycle, and tandem), on the other hand, must discretize a 2D domain and determine values for both L_z and L_x that are sufficiently large. Although the inclusion of a volume discretization enables the consideration of more complex material properties (e.g., heterogeneities, inelasticity), they are inherently more computationally expensive than those based on BEM, making the exploration of computational domain size an expensive task. To ease computations, all of these volume-based codes (with the exception of SPEAR, which considers a constant cell size throughout the domain) utilize a grid stretching, in which high resolution can be localized in a region around the fault. Some codes accomplish this by defining the minimum cell size Δ in the vicinity of the frictional portion of the fault and gradually coarsening in both the directions up to the maximal cell size of Δ_{max} . Cell size is not required to be the same in both the x- and z- directions, but all codes chose to do so. Others use a constant cell size in a region around the fault defined by length scales ℓ_x and ℓ_z (see Fig. 1). For both the benchmark problems, we report on choices for domain sizes (that prove sufficiently large) and grid-coarsening techniques used.

COMPARISONS OF SIMULATION RESULTS

In the sections and figures that follow, we showcase comparisons across codes for both BP1-FD and BP3-QD. Labels in the figures provide information on the code used for the simulation results, along with possible exceptions to parameters used (e.g., changes in specified cell size), or information on computational domain size choices.

As will be shown, except for a few outliers, we obtain qualitatively good agreements across codes in the sense that different codes produce similar distributions and values for short-term, coseismic properties (e.g., peak slip rates, stress drops, rupture speeds, and coseismic surface displacements), as well as long-term features (e.g., number of characteristic events, recurrence times, magnitudes, nucleation locations, and off-fault surface displacements), which remain comparable (by visual inspection) throughout the simulation period.

Quantitative metrics

To refine our visual assessments of model comparisons, we define long- and short-term metrics. The latter are informed by metrics used within the dynamic rupture community, namely, those defined in Day *et al.* (2005) and Barall and Harris (2014). First, a well-resolved reference solution is computed using one code from each benchmark problem, namely

BICyclE (for BP1-FD) and Unicycle (for BP3-QD, only the 30° thrust-faulting scenario). These codes were chosen for their computational efficiency compared to volume-based codes. For BP1-FD, the reference solution R_1 is obtained using a cell size of $\Delta z = 6.25$ m and a computational domain size $L_z = 200$ km. For BP3-QD, the reference solution R_2 uses $\Delta z = 12.5$ m; by design, Unicycle considers a semi-infinite domain. For both the benchmark problems, we ascertain self-convergence by computing the error made with the reference solution, starting with a large cell size that is successively halved. For BP1-FD, we utilize an additional reference solution R_3 corresponding to $\Delta z = 12.5$ m and $L_z = 240$ km, which enables self-convergence studies when starting with a small domain size that is successively increased. Details of these self-convergence tests are provided in the supplemental material.

The three reference solutions for each benchmark problem are used to explore sensitivity to cell size and domain size, and also to compare results from participating codes. For long-term quantitative comparisons, we define two metrics: the percent error in interevent timing and the percent error in moment over the entire simulation period. For example, if event n of the reference solution nucleates at time T_n since the last event (determined when max slip rate in an interseismic period first exceeds 10^{-3} m/s), and a comparative model result nucleates at time \tilde{T}_n , then the percent error is given by

%error : Time between events =
$$|T_n - \tilde{T}_n|/|T_n| \times 100$$
. (9)

The percent error in moment is computed similarly, in which moment for a specific event defined over $t_1 \le t \le t_2$ is defined by $\int_0^{W_f} \mu[\delta(z',t_2) - \delta(z',t_1)]dz'$, in which the dummy variable z' varies over distance down-dip (i.e., z in BP1-FD and x_d in BP3-QD) in the frictional section of the fault $(0,W_f)$.

For short-term quantitative comparisons, we focus on one particular event within the simulation, and compute the L^2 -norm (integrated-) error in slip or slip-rate time series at a specific location. We first align the time series from a certain model with the reference solution by finding the best time shift that maximizes the cross correlation of the two time series. For example, if $V_{\rm ref}(t)$ and $\tilde{V}(t)$ are the reference and (shifted) comparative slip rates, respectively, then we compute the relative error (expressed as a percent), defined by

$$\%\text{err}(V) = ||V_{\text{ref}} - \tilde{V}||/||V_{\text{ref}}|| \times 100, \tag{10}$$

in which the norm is defined for a fault variable g at a specific location by $||g||^2 = \int_0^T |g(t)|^2 dt$, in which T = 30 s and integrals are approximated with trapezoidal quadrature. The corresponding percent error for slip $\%\text{err}(\delta)$ is defined similarly. The time shift minimizes the L^2 -error, which is computed by interpolating to the temporal locations of the reference solution and computed over a 30 s time window starting at the time at which

the slip rate of the reference solution at that fault location first exceeds 10^{-3} m/s.

Another metric that we compute is percent error associated with rupture arrival time of a certain event, relative to the nucleation time. We define event nucleation to be when the slip rate near the nucleation depth (at or around 12.5 km down-dip for all simulations) first exceeds the specified threshold (which we take to be 10^{-3} m/s). If $t_{\rm ref}$ and \tilde{t} are the rupture arrival times at a particular fault location, then the percent error is given by

%error : Rupture arrival time =
$$|t_{ref} - \tilde{t}|/|t_{ref}| \times 100$$
. (11)

This metric enables the quantitative comparisons of individual rupture features, independent of absolute nucleation time.

Sensitivity to cell size and domain size

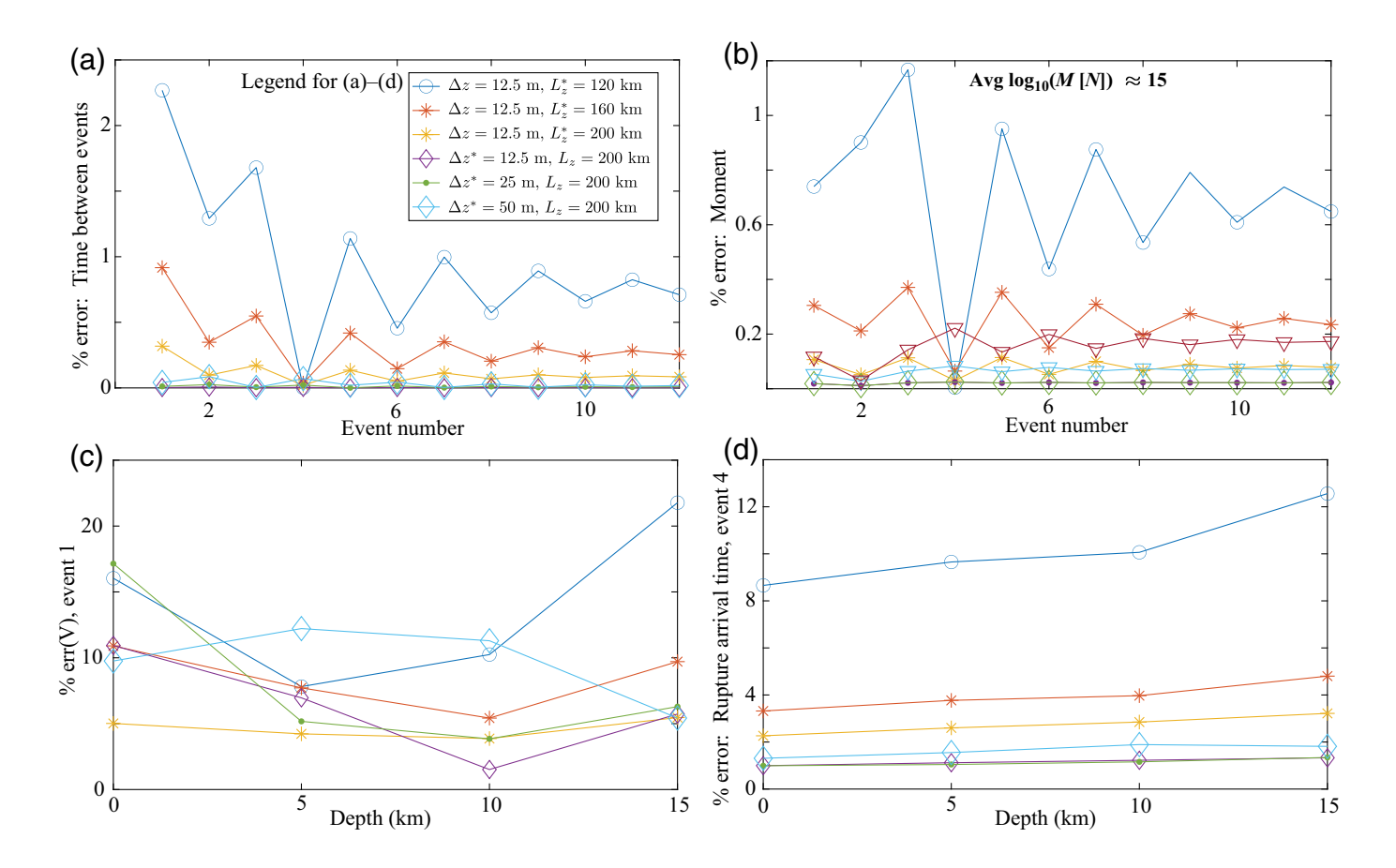
We first apply both long- and short-term metrics to the results from the BICyclE code (for BP1-FD) used to compute the reference solutions to explore sensitivity to cell size and domain size shown in Figure 2, in which the asterisks in the legend refer to error computed against a particular reference solution R_1 or R_3 . Figure 2a,b shows percent errors in interevent time and moment, illustrating that these errors are more sensitive to smaller computational domain size than to the cell sizes considered. When using a domain size of $L_z=200$ km, a cell size smaller than 50 m is sufficient to yield errors well below 1% in both the cases. When using a cell size of 12.5 m, a computational domain size $L_z \geq 160$ km is sufficient in achieving percent errors below 1%.

For coseismic metrics, shown in Figure 2c,d, we consider the first and fourth events, respectively. Figure 2c is %err(V) at different distances down-dip, with values ranging from about 2% to 20%. A 20% error corresponds roughly to a difference between 1 and 1.2 m/s peak slip rate. In this case, both small domain sizes and large cell size contribute significantly to error. Percent errors are small for the case of $\Delta z=12.5\,$ m, $L_z=200^*\,$ km, but this is relative to a larger computational domain (reference solution R_3), indicating that errors for slip rates are not that sensitive when increasing L_z above 200 km. On the other hand, the error made when computing relative to a small cell size (reference solution R_1) is slightly larger, at least at some depths, indicating that coseismic slip rates are more sensitive to spatial resolution. Figure 2d shows percent error in rupture arrival time, with results more sensitive to computational domain size.

In the sections that follow, we compare model results across codes and assess agreement based on visual inspection. We then present quantitative errors made via the metrics defined in this section.

BP1-FD model comparisons

BP1-FD constitutes our first benchmark problem that considers fully dynamic earthquake ruptures. To illustrate the differences



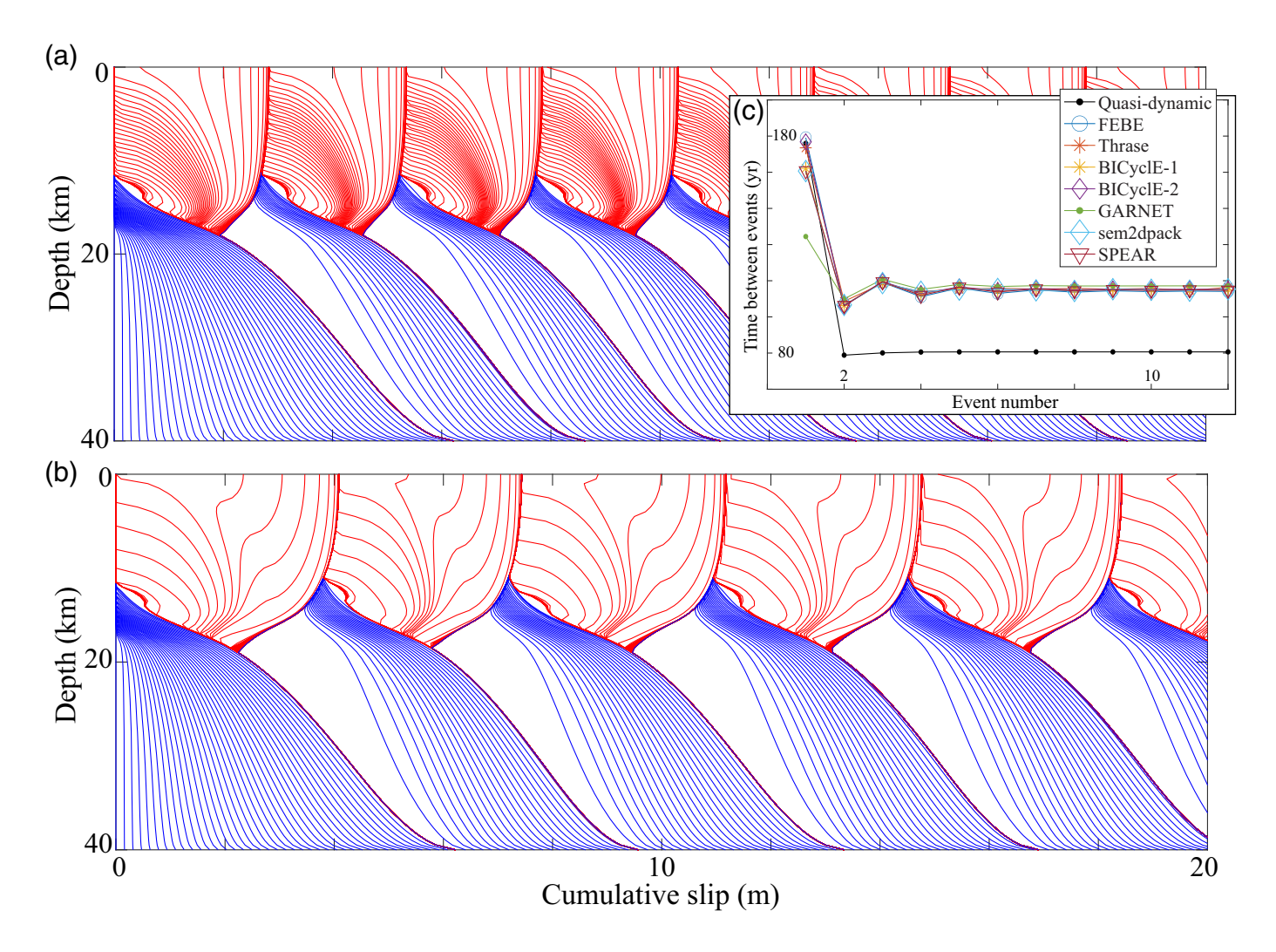
when including full elastodynamics, Figure 3 presents results from BP1-QD and BP1-FD using the BICyclE code (Lapusta et al., 2000; Lapusta and Liu, 2009). In Figure 3a,b, cumulative slip profiles are plotted in blue contours every year during interseismic loading (when the max slip rate <1 mm/s) and in red contours every 1 s during coseismic rupture. Figure 3c shows calculated recurrence times across all the codes, showing good agreements. Also shown are recurrence times from BP1-QD using the BICyclE code. These figures showcase that although both benchmark problems involve characteristic event sequences (after a spin-up period consisting of $\sim 1-2$ events), nucleating at a similar depth of ~12 km, the inclusion of full dynamics shows more slip with each earthquake, corresponding to larger magnitudes and longer recurrence times (~120 vs. 78 yr)—a marked reflection off the free surface (missing from the quasidynamic simulation), higher slip rates, and rupture speeds (evidenced by the vertical and horizontal spacing of red contours, respectively, as discussed in Thomas et al., 2014).

For the volume-based and hybrid codes participating in BP1-FD, details of the computational parameters used are provided in Table 4, including values for L_x and L_z , order of spatial accuracy p, and minimum cell size Δ , used within the vicinity of the fault. Some codes did not use the suggested cell size of 25 m but increased it to 50 m (to ease computational cost), thus resolving length scales in equations (6) and (7) with half the number of grid points (6 and 40, respectively). Also reported are details of the grid-coarsening techniques that were used.

Figure 2. Percent errors in (a) interevent times, (b) event moments (in which the average moment is $\log_{10}(M[N]) \approx 15$), (c) integrated slip rate during event 1, and (d) rupture arrival time when using the BICyclE code for BP1-FD and successively halving the cell size Δz or increasing computational domain size L_z . Asterisks in the legend refer to the reference solution against which the error is computed: An asterisk on cell size Δz means reference solution R_1 , and asterisk on L_z means reference solution is R_3 . The color version of this figure is available only in the electronic edition.

The SBEM-based BICyclE code uses a computational domain depth of $L_z=160~\rm km$ and a cell size of 25 m. In light of the quantitative sensitivity analysis discussed in the section on Sensitivity to cell size and domain size, these choices should produce reasonable results.

Some codes for BP1-FD naturally handle the seamless transition between quasi-static and fully dynamic treatments of the equations of motion throughout all phases of earthquake sequences (e.g., the BICyclE code of Lapusta et al., 2000). The volume-based code GARNET also seamlessly integrates the elastodynamic equations throughout the entire simulation by utilizing adaptive, implicit time stepping. However, the remaining volume-based codes of this study assume negligible inertial effects during the interseismic phases and integrate the quasi-static equations with explicit, adaptive time stepping. At the onset of event nucleation, however, inertia is no longer negligible, and the elastodynamic equations must be considered. Thus, a switching criterion must be implemented, transitioning



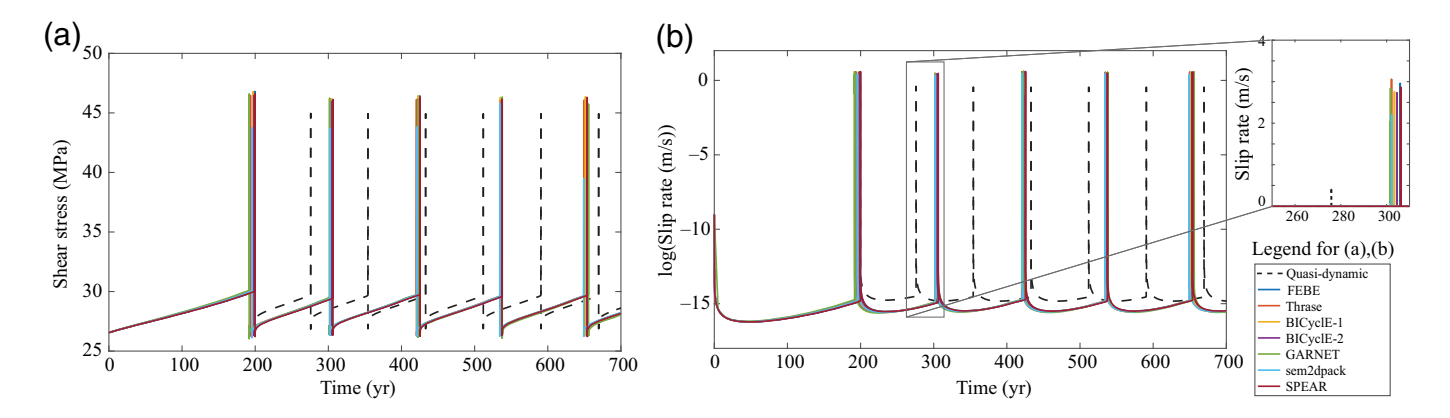
from the adaptive time stepping involved in a quasi-static solver to a small (often constant) time-step, explicit integration technique for the dynamic rupture phase. For example, Thrase switches between solvers based on the maximum slip rate on the fault, whereas other switching criterion based on a nondimensional parameter R (the ratio of the radiation damping term to the quasi-static stress) exist Duru *et al.* (2019).

Model sensitivity to the switching criterion was left to be explored by individual modeling groups. Table 4 includes information on the strategy used by these volume-based codes, along with the threshold parameter(s) that enabled matching results. example, Thrase uses the maximum slip rate criterion, switching from a quasi-static to a dynamic solver when max(V) > 10 mm/s and back to quasi-static once max(V) <1 mm/s. Such a choice is denoted max(V,10,1) in the Table 4, which illustrates that all codes utilizing this max(V) criterion use nonsymmetric threshold parameters, requiring more stringent criteria for switching back to quasi-static solver. We found in most cases that switching from quasi-static to dynamic was less sensitive to the threshold parameter than switching back; switching too abruptly back to the quasi-static solver can lead to large step changes in shear stress and slip rates, or can lead to frequent switching between solvers due to

Figure 3. Cumulative slip profiles for (a) BP1-QD and (b) BP1-FD plotted in blue contours every 5 yr during the interseismic phases and in red every second during coseismic rupture. BP1-QD results taken from the BICyclE code, with $L_z=160$ km. After a spin-up period of approximately two events, characteristic event sequences emerge for both BP1-FD and BP1-QD. (c) Recurrence times for BP1-FD (\sim 120 yr) across all codes and for BP1-QD (\sim 78 yr). The color version of this figure is available only in the electronic edition.

oscillations in slip rate near the end of a dynamic rupture (Harvey *et al.*, 2022). Also included in Table 4 are boundary conditions assumed at the finite-domain edges $\pm L_x$, L_z truncating the half-space, during the quasi-static regime, in which "QSBC" stands for the boundary condition type: "disp, free" refers to a displacement condition at $x = \pm L_x$, and a traction-free condition at $z = L_z$. During the dynamic phases, all codes used nonreflecting conditions at these boundaries.

Just as for BP1-QD, sufficiently larger domain sizes yield good agreements across codes, as seen in Figure 4 in which long-term time series of shear stress and slip rate (at 7.5 km depth) are shown for the best model results. Also plotted for comparison are the corresponding time series for the quasidynamic simulations of BP1-QD from the BICyclE code. The



fully dynamic simulations are accompanied with higher shear stresses due to higher slip rates; at this depth, the fully dynamic simulations reach the maximum slip rate of ~ 3 m/s, compared to ~ 0.5 m/s in the quasi-dynamic simulation. Higher slip rates in the fully dynamic simulations are caused by a much larger wave-mediated dynamic stress concentration and accompanied with a higher stress drop, leading to the increased recurrence times compared with the quasi-dynamic simulation.

We also compared coseismic time series corresponding to the fourth event in BP1-FD, shown in Figure 5. Time (in seconds) is relative to the time at which the slip rate near the nucleation depth (z=12.5 km) first exceeds 10^{-1} m/s (which corresponds to a different temporal shift for different model results). Figure 5a shows fault shear stress at z=12.5 km across modeling groups, along with the corresponding time series for the quasi-dynamic simulation BP1-QD. The orange curve of Thrase illustrates the step change in shear stress that can occur when switching back to the quasi-static solver too abruptly (however, in this case the step change does not significantly alter the long-term agreements with the other model results). Figure 5b is the slip rate at z=7.5 km across codes along with those from BP1-QD (also in black). The quasi-dynamic simulation exhibits a lower stress drop and an overall decrease in

Figure 4. Long-term behavior of BP1-FD models. (a) Shear stress and (b) slip rates at the depth of 7.5 km across codes with sufficiently large computational domain sizes. Also shown (in dashed black) are those for the quasidynamic counterpart BP1-QD. The color version of this figure is available only in the electronic edition.

slip rate at these depths. Showcasing time series at the two different depths enables an estimate of rupture speed: the quasidynamic event propagates more slowly, as illustrated by the later arrival of the surface reflection phase (marked by a black arrow): ~ 0.4 km/s versus ~ 1.25 km/s for the fully dynamic rupture.

The quantitative errors associated with BP1-FD are shown in Figures 6 and 7. Encouragingly, for long-term comparisons errors across all codes remain persistently less than 5% over the simulation period, as shown in Figure 6. For coseismic comparisons, Figure 7a illustrates how the time series of a comparison model (SPEAR) is shifted and interpolated to minimize the integrated error %err(V) against the well-resolved reference solution R_1 . The zoom in Figure 7a is done to reveal where discrepancies between results contribute to errors. Figure 7b,c shows %err(V) and %err(δ) across all codes during event 4.

TABLE 4	
Computational Parameters and Methods Used in Volume-Based	I Codes for BP1-FD and BP3-QD, Unless Otherwise Noted

Code Name	L _x ,L _z	р	Δz	Grid Coarsening	QSBC	Switching
BP1-FD						
FEBE	n/a, 160 km	2	25 m	n/a	n/a, free	$R = 10^{-4}$
GARNET	160, 80 km	8	25 m	$\Delta_{\sf max} = 200 \; {\sf m}$	n/a	n/a
sem2dpack	160, 160 km	4	25 m	$\Delta_{max} = 500 \; m$	disp, free	max(V,3,2)
Thrase	160, 160 km	4	50 m	$\ell_x, \ell_z = 125 \text{ km}$	disp, free	max(V,10,1)
SPEAR	160, 160 km	5	50 m	n/a	disp, free	max(V,5,2)
BP3-QD						
sbplib	150, 100 km	6	100 m	$\ell_{x}, \ell_{d} = 5,45 \text{ km}$	disp, free	n/a
FDCycle		4		$\ell_x \ell_d = 40 \text{ km}$	disp, free	n/a
$(\psi = 90^{\circ})$	400, 400 km		100 m	X. C	• •	n/a
$(\psi = 60^{\circ})$	100, 100 km					n/a
$(\psi = 30^{\circ})$	200, 200 km		200 m			n/a
Tandem	3400, 3400 km	8	31.25 m	$\Delta_{\text{max}} =$ 12.5 km	disp, free	n/a

BP1-FD codes utilizing a switching method are defined by type and parameters; see section BP1-FD model comparisons for more details. QSBC, Quasi-static boundary condition.

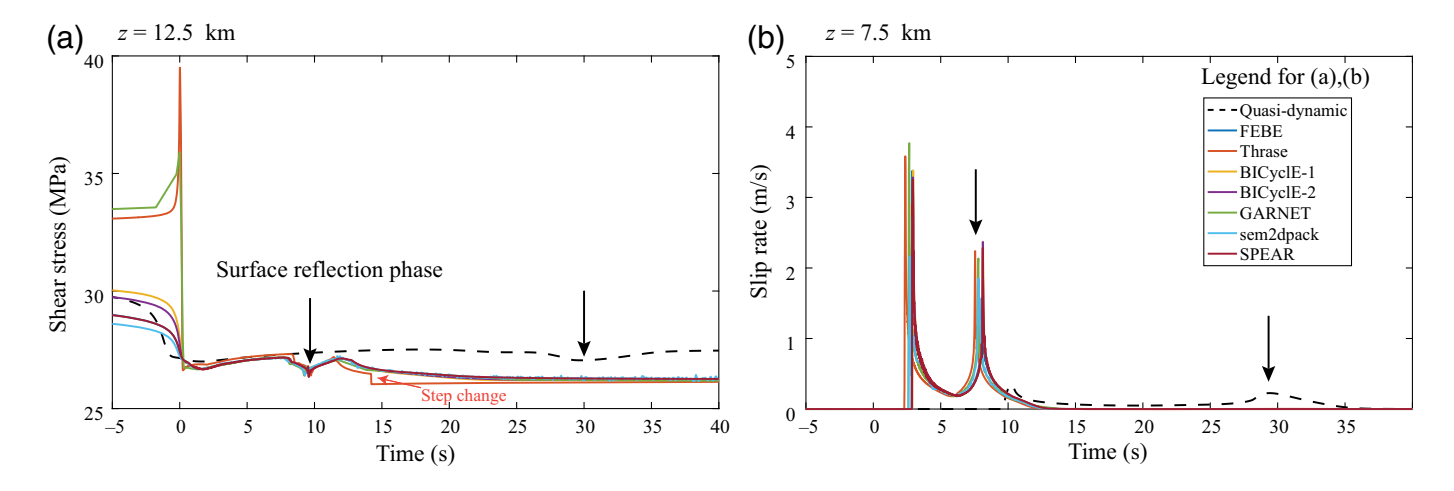


Figure 5. Coseismic behavior of BP1-FD across codes with sufficiently large computational domain sizes during the eighth event, shown for (a) shear stresses at 12.5 km depth and (b) slip rates at 7.5 km depth. Also shown (in dashed black) are those for the quasi-dynamic counterpart BP1-QD. Time (in seconds) is relative to the time at which the slip rate near the nucleation depth (z = 12.5 km) first exceeds 10^{-1} m/s; the eighth QD event occurs a

few hundred years before the eighth FD event. The surface reflection phase is marked by a black arrow. The orange arrow in panel (a) illustrates how a step change in shear stress can occur (in this case for the Thrase code) when switching abruptly back to a quasi-static solver. The color version of this figure is available only in the electronic edition.

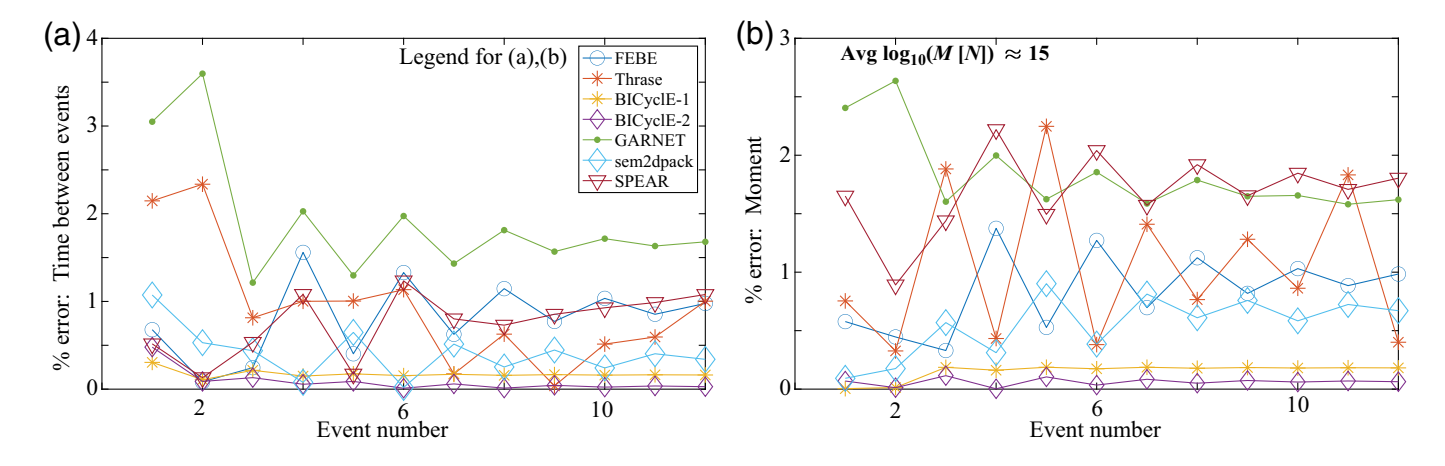


Figure 6. Long-term metric comparisons for BP1-FD show percent errors in interevent times (a) and moment (b) plotted against event number, in which error is relative to the reference solution R_1 (with average magnitude

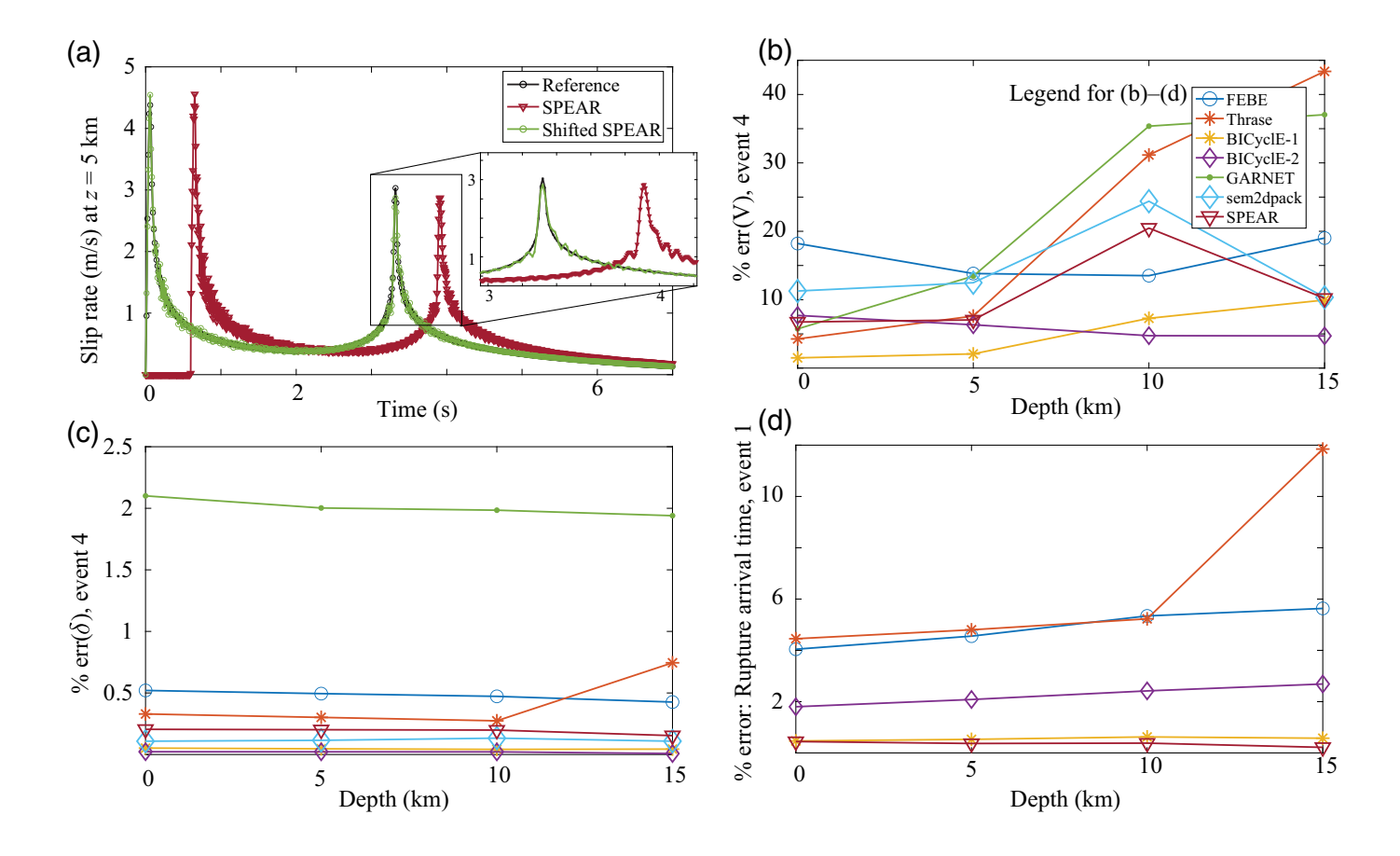
 $\log_{10}(M[N]) \approx 15$). The color version of this figure is available only in the electronic edition.

Although errors in slip rate range from about 2% to 40%, errors in slip are only a few percent. Such large errors in slip rate arise due, in part, to interpolation of time steps and also due to different problem formulations, numerical methods, and parameters, and so on. In addition to time shifting, these latter errors could potentially be further minimized by applying a low-pass filtering (as done in Barall and Harris, 2014). However, the range of percent errors we find are in line with the percent errors computed in dynamic rupture simulations Day *et al.* (2005), in which errors in peak slip rates range from ~18% to 38%. In Figure 7d, we plot percent error in rupture arrival time during event 1 (for only a subset of models in which

output data are sufficiently sampled) and compute errors at or well below 10%.

BP3-QD model comparisons

The 2D plane strain scenario of BP3-QD comes at a higher computational cost than the antiplane shear scenarios of earlier benchmarks BP1-QD and BP2-QD. The suggested cell size of 25 m was not feasible for all participating volume-based codes, and not having a priori knowledge of sufficiently large domain size requirements added to modeling efforts; thus, we did not conduct an in-depth study on what constitutes a sufficiently large domain. However, in the following paragraphs we share model



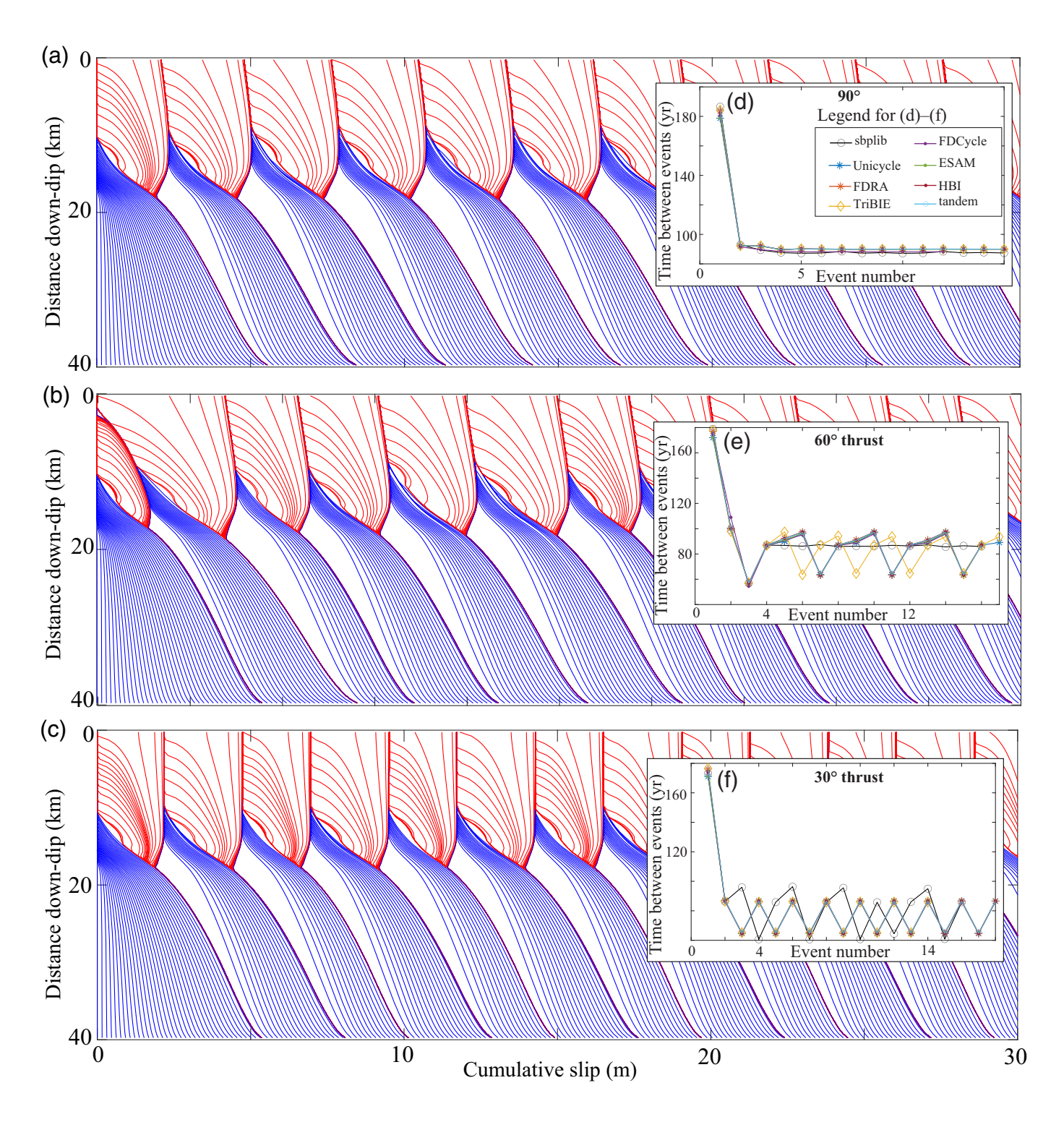
results, and in nearly all cases we obtain good agreements across codes. Some outliers exist that diverge from the others after the first few events, which is not unexpected, as simulation results tend to diverge over time due to round-off error and/or due to differences in domain size choices or other numerical features such as order of accuracy and cell size (Erickson *et al.*, 2020; Lambert and Lapusta, 2021). Where qualitative differences exist, we note these outliers and shed light on possible sources of discrepancies in the last part of this section.

As in BP1-FD, the volume-based codes discretize a 2D domain, and thus also choose values for both L_z and L_x . Table 4 provides an overview of choices made by the volume-based codes, including computational domain sizes (L_r and L_z), spatial order of accuracy p, and choice of boundary condition type, in which "disp, free" refers to a displacement boundary condition at $x = \pm L_x$ and a traction-free condition at $z = L_z$. Cell sizes used are as large as 200 m, which resolves length scales in equations (6) and (7) with 2 and 12.5 grid points, respectively. Also included in Table 4 are details of grid-coarsening techniques implemented to ease the computational costs. Although not explored by all the volume-based codes, tandem has found that rather aggressive grid stretching away from the fault may be permissible (Uphoff et al., 2022), which might be due, in part, to the more forgiving nature of quasi-dynamic models that do not suffer the same dispersion errors as fully dynamic simulations.

We first use BEM-based model results to illustrate the types of behaviors that emerge with differing dip angles. Figure 8a-c

Figure 7. Short-term metric comparisons for BP1-FD focus on a single coseismic event and shift all comparative time series to minimize errors, as illustrated in (a) for the SPEAR code, for reference solution R_1 . Percent errors shown against depth for (b) integrated slip rate and (c) slip during event 4, and for (d) rupture arrival time during event 1. The color version of this figure is available only in the electronic edition.

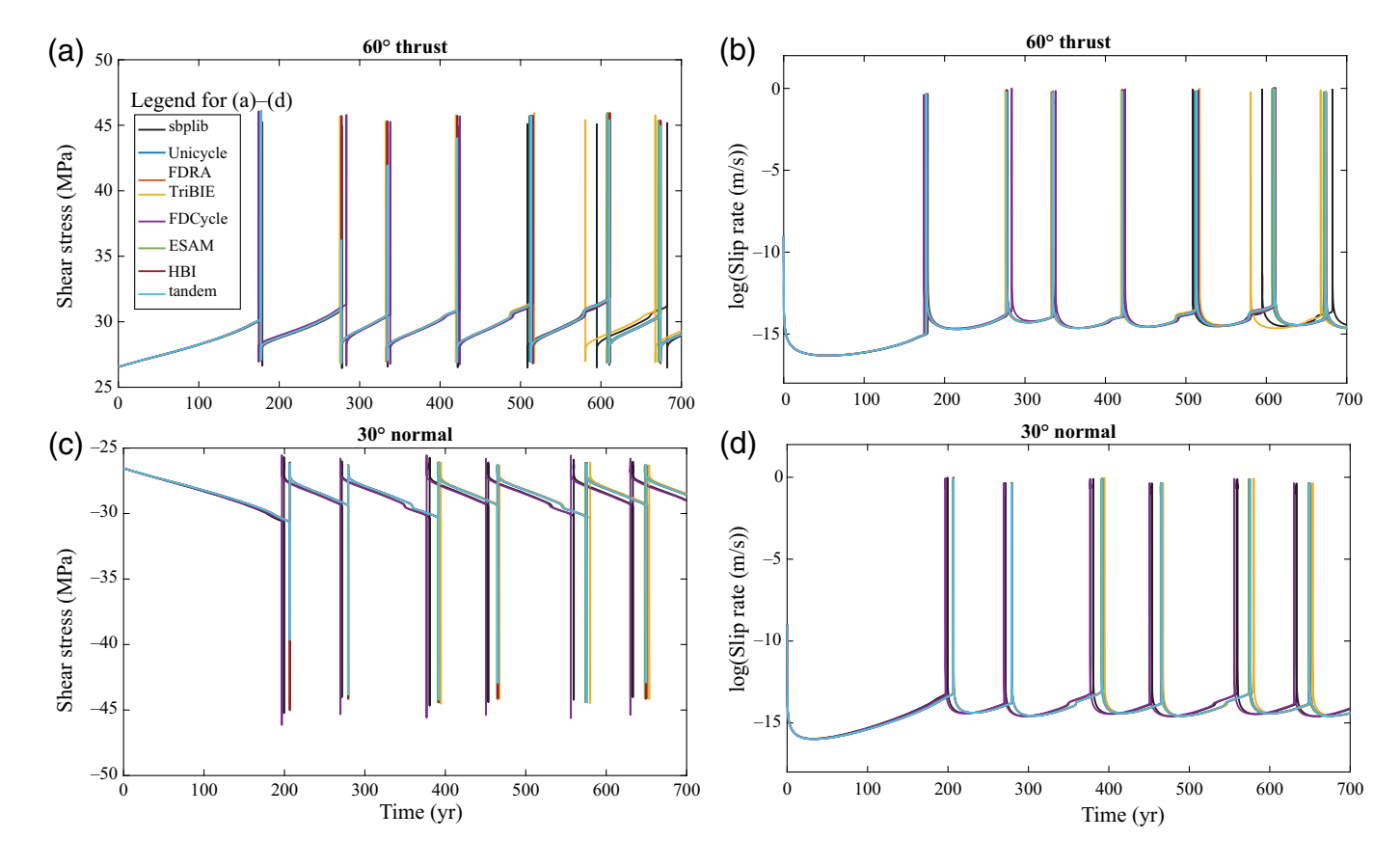
shows cumulative slip versus distance down-dip for each of the thrust fault scenarios, with blue contours plotted every year during the interseismic period (when the max slip rate <1 mm/s) and in red every second during coseismic rupture. Analogous plots for the normal-faulting cases are contained in the supplemental material. All scenarios in Figure 8a-c involve only surface-rupturing events, all nucleating at or close to 12 km down-dip. To better understand these event sequences, in Figure 8d,e we plot the corresponding interevent times across codes. Barring a few outliers (sbplib and TriBIE in Fig. 8e and sbplib in Fig. 8f), good agreements are obtained across codes. These figures reveal that the 90° (vertical) case exhibits one characteristic event, nucleating every ~90 yr. For the 60° thrust-fault scenario, four characteristic events emerge with interevent times of ~60, 87, 90, and 95 yr, with longer interevent times corresponding to larger events. The 30°-thrust case exhibits two characteristic events with interevent times ~65 and 80 yr. For the normal-faulting scenarios, results across codes exhibit good agreements, barring some slight discrepancies in the results of



FDCycle and sbplib, as detailed in the supplemental material. A better understanding of the influence of fault dip angle and sense of motion on the variability of earthquake sizes is warranted and would require a larger exploration of the parameter space.

Time series of shear stress and slip rate at the down-dip distance $x_d = 7.5$ km are shown in Figure 9 for several representative cases of thrust and normal faulting (and dip-angle) scenarios across all the participating codes. Remaining cases as well as long-term time series of normal stresses are contained in the supplemental material. As shown in Figure 9, in nearly all

Figure 8. Cumulative slip profiles for BP3-QD thrust-faulting simulations from the FDRA code with dip angles (a) 90° , (b) 60° , and (c) 30° plotted in blue contours every 5 yr during the interseismic phases and in red every second during coseismic rupture. Interevent times for corresponding simulations across all participating codes shown in (d) for 90° , in which characteristic events emerge every ~ 90 yr; (e) for 60° , in which four distinct event types emerge every ~ 60 , 87, 90, and 95 yr; and (f) for 30° , in which two characteristic events emerge every ~ 65 and 80 yr. The color version of this figure is available only in the electronic edition.



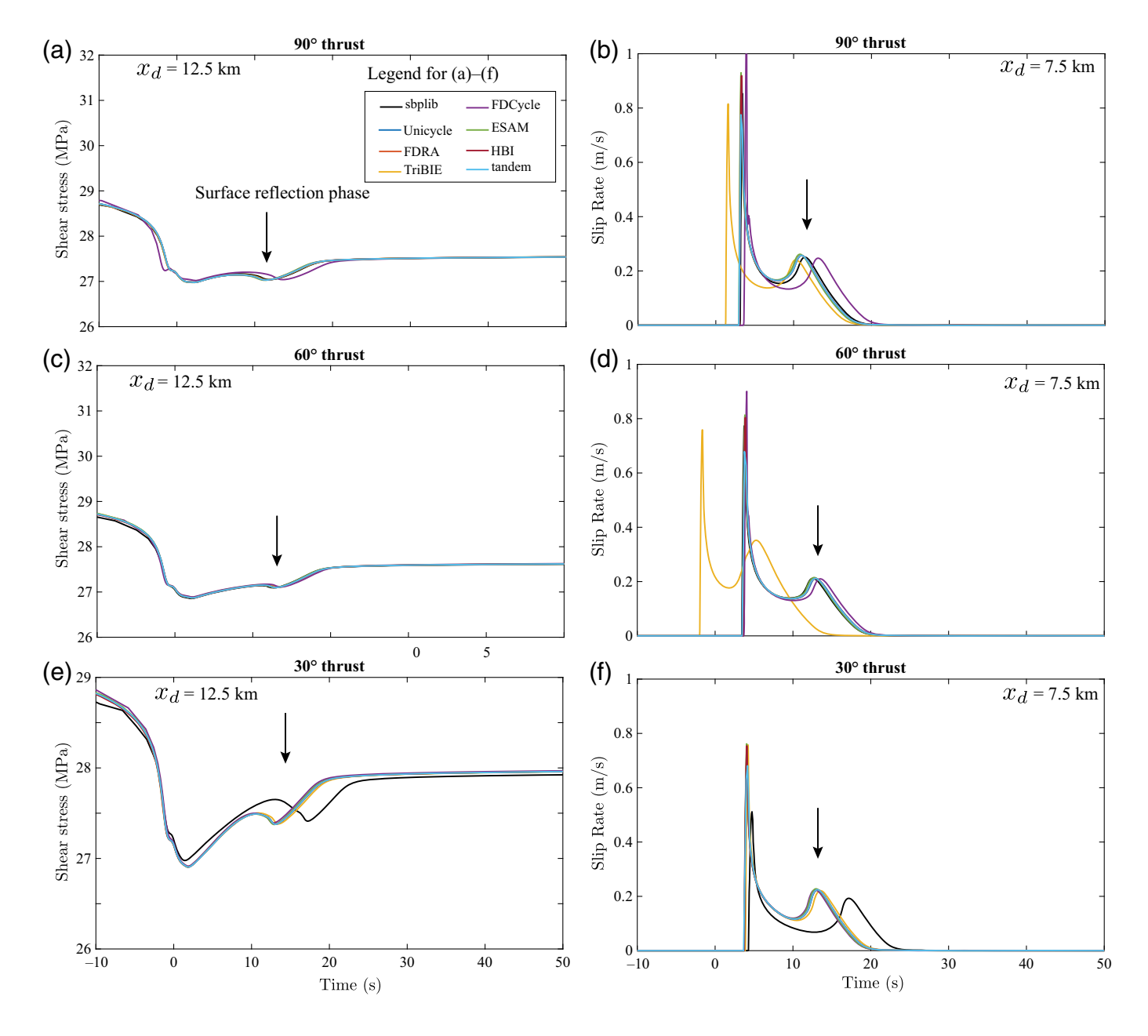
cases the results show good agreements, barring the few outliers previously mentioned. The outliers in the 30° normal-faulting scenarios (FDCycle and sbplib) match each other and agree qualitatively with the others in the sense that the numbers of characteristic events agree. However, there are small but noticeable differences in the interevent times. We explore these discrepancies further in the last part of this section.

Next, we consider coseismic rupture time series plotted in Figures 10 and 11 across all the codes. We plot shear stress at the down-dip distance $x_d = 12.5$ km for the fourth event in each sequence, with time relative to that when the slip rate at this distance down-dip first exceeds 10⁻¹ m/s. Slip rate further up-dip (at $x_d = 7.5$ km depth) is also plotted in Figures 10 and 11, which enables an estimate of rupture speed. Barring the outliers noted previously, there is a widespread agreement across codes in terms of peak stress and slip rate values, and features of the coseismic reflection (noted by a black arrow in the figures). For the thrust-fault scenarios, rupture speeds (illustrated by the arrival of the surface reflection phase) do not appear to be significantly affected by dip angle; however, the maximum slip rates decrease slightly with dip angle, at least at this distance down-dip. For normal faulting, maximum slip rates also decrease with dip angle, and the rupture speed of the 60° simulation appears higher than that of the 30°. To better understand the dependency of rupture characteristics on dip angle warrants further study.

As a final comparison, we consider time series of surface stations across codes, plotted for several representative cases

Figure 9. Long-term time series of shear stress and slip rate for representative BP3-QD-faulting scenarios at $x_d=7.5\,$ km for (a,b) 60° thrust and (c,d) 30° normal cases. The color version of this figure is available only in the electronic edition.

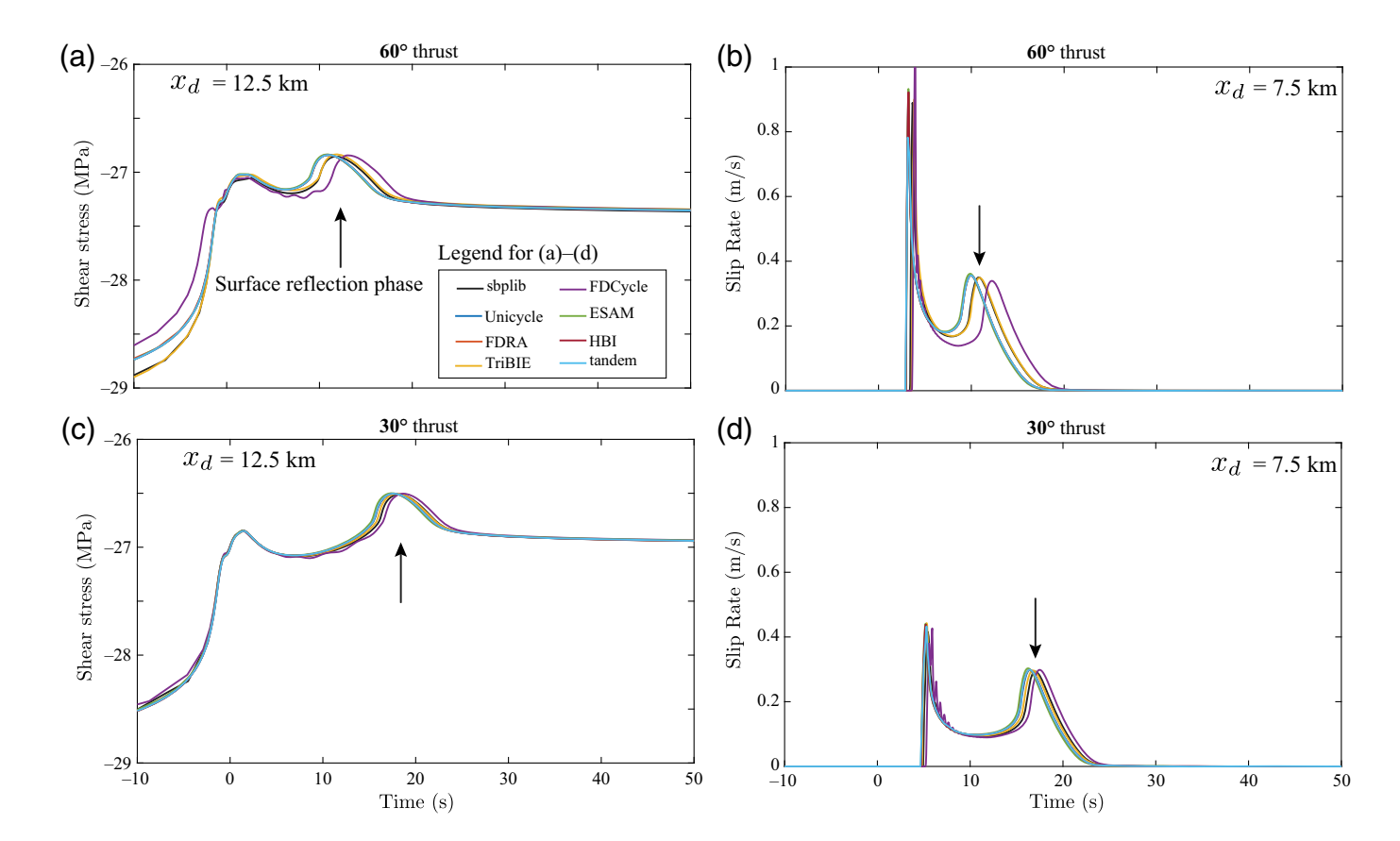
in Figure 12, with all the remaining cases included in the supplemental material. For this benchmark, we requested time series of surface displacements and velocities at distances $x = 0^+, x = \pm 8, \pm 16$, and ± 32 km from the fault trace. Here, we only compare surface displacements, because some codes do not compute velocities (and some codes do not compute either, hence only a subset of participating codes are plotted here). As mentioned previously, early simulations results revealed major discrepancies across codes brought on by an initial ambiguity in the benchmark problem statement, because we did not specify boundary conditions at infinity. After addressing this ambiguity (i.e., adding the condition in equation 8), good agreements across codes are obtained. Figure 12 shows both horizontal and vertical components of surface displacement at distances $x = 0^+$ km (in thick solid lines) and $x = \pm 16$ km (in thin dashed lines) are shown. We also include (for reference) data for $x = 0^-$, but only from FDCycle (in thin solid lines), as it was not requested in the benchmark description. Stations at distances from the fault trace tend toward the rigid body translation, which we plot (for reference) in yellow and mark with text to indicate motion on the hanging or foot wall.



For the 90° thrust-faulting case, shown in Figure 12a,d, the horizontal components of displacement all fluctuate near or around 0 m (the rigid body motion). The vertical displacements are antisymmetric about x = 0, with higher velocities (i.e., larger gradients in displacement per earthquake) at stations closer to the fault trace. For the nonvertical-dipping fault cases, both the components of displacements reveal asymmetries about x = 0. For both thrust and normal faulting, a dip angle of 60° results in lower total displacements but higher velocities in the horizontal components on the foot wall $(x \le 0)$ at stations near the fault trace, shown in Figure 12b, c,e,f, respectively. On the hanging wall $(x \ge 0)$, the horizontal ground motions approximately track the rigid body translation, whereas vertical components of velocity (i.e., the gradient of displacement time series) are higher for stations near the fault trace, which experience less total displacement. These

Figure 10. Coseismic behavior of BP3-QD models during the eighth event for thrust-fault cases. Barring a few outliers, good agreements across codes exist for shear stresses at $x_d = 12.5$ km and slip rates at $x_d = 7.5$ km for (a,b) 90°, (c,d) 60°, and (e,f) 30°. Time (in seconds) is relative to the time at which the slip rate near the nucleation location ($x_d = 12.5$ km) first exceeds 10^{-1} m/s. The surface reflection phase is marked by a black arrow. The color version of this figure is available only in the electronic edition.

features largely align with the findings of Duan and Oglesby (2005) for the nonvertical-dipping faults, in which the horizontal component of ground motion was observed to dominate on the foot wall, whereas the vertical component dominates on the hanging wall. We find that for the 30°-dipping thrust and normal fault scenarios (supplemental material), the horizontal components of velocity are higher on the hanging wall at



stations closer to the fault trace, whereas the foot wall more closely tracks the rigid body translation.

To compute quantitative errors associated with BP3-QD, we utilize the Unicycle reference solution R_2 for the 30° thrust-fault scenario. Errors across participating codes associated with the long- and short-term metrics are given in Figures 13 and 14. As in BP1-FD, percent errors for long-term features across all codes remain below 5% (for interevent times) and below 10% (for moments) over the simulation period, as shown in Figure 13. For quantitative coseismic comparisons, Figure 14a illustrates that, even with time shift, the main and reflective phases have significant mismatch, not to mention that the time series from FDCycle contains more oscillations (most likely numerical artifacts). Figure 14b,c shows %err(V) and %err(δ) during event 1 at different distances down-dip, across all codes; we found that such errors persist for later events. As in BP1-FD, errors in slip rate range from about 2% to 40%, whereas errors in slip remain well below 8%.

In Figure 14d, we plot percent error in rupture arrival time during event 4, for all participating codes. The codes spblib and FDCycle were already identified to contain more discrepancies than others, with percent errors between 5% and 20%. Other codes, however, contain percent errors well below 5%.

Reducing discrepancies in BP3-QD

The computational load of BP3-QD means that exploring numerical dependencies on results (in particular, computational domain size) is an expensive task. In an ideal scenario,

Figure 11. Coseismic behavior of BP3-QD models during the eighth event for normal fault cases. Good agreements across codes exist for shear stresses at $x_d = 12.5$ km and slip rates at $x_d = 7.5$ km for (a,b) 60° and (c,d) 30°. Time (in seconds) is relative to the time at which the slip rate near the nucleation location ($x_d = 12.5$ km) first exceeds 10^{-1} m/s. The surface reflection phase is marked by a black arrow. The color version of this figure is available only in the electronic edition.

we would explore dependency on both L_z and L_x in a volumebased code, using a small cell size, but this is currently not computationally feasible. In cases in which volume-based model results do not match the best BEM results in all cases, sources of discrepancies are attributed at least, in part, to cell size and computational domain size, but other errors (from numerical choices such as time stepping) also likely contribute. To better understand some of these sources of error, in Figure 15, we focus on the 60° normal-faulting case and compare results from the volume-based code FDcycle to a reference solution (here, we choose to use the BEM-based code FDRA, as, similarly to Unicycle, it uses a small cell size of 25 m and considers a semi-infinite spatial domain). Figure 15a shows long-term time series of slip rate downdip at $x_d = 12.5$ km for both the codes, with FDCycle assuming different values for the computational domain size and numerical parameter choices (with order of accuracy p = 4, unless noted otherwise). For small domain sizes, major discrepancies are evident (two characteristic events emerge compared to the single characteristic event sequence in the

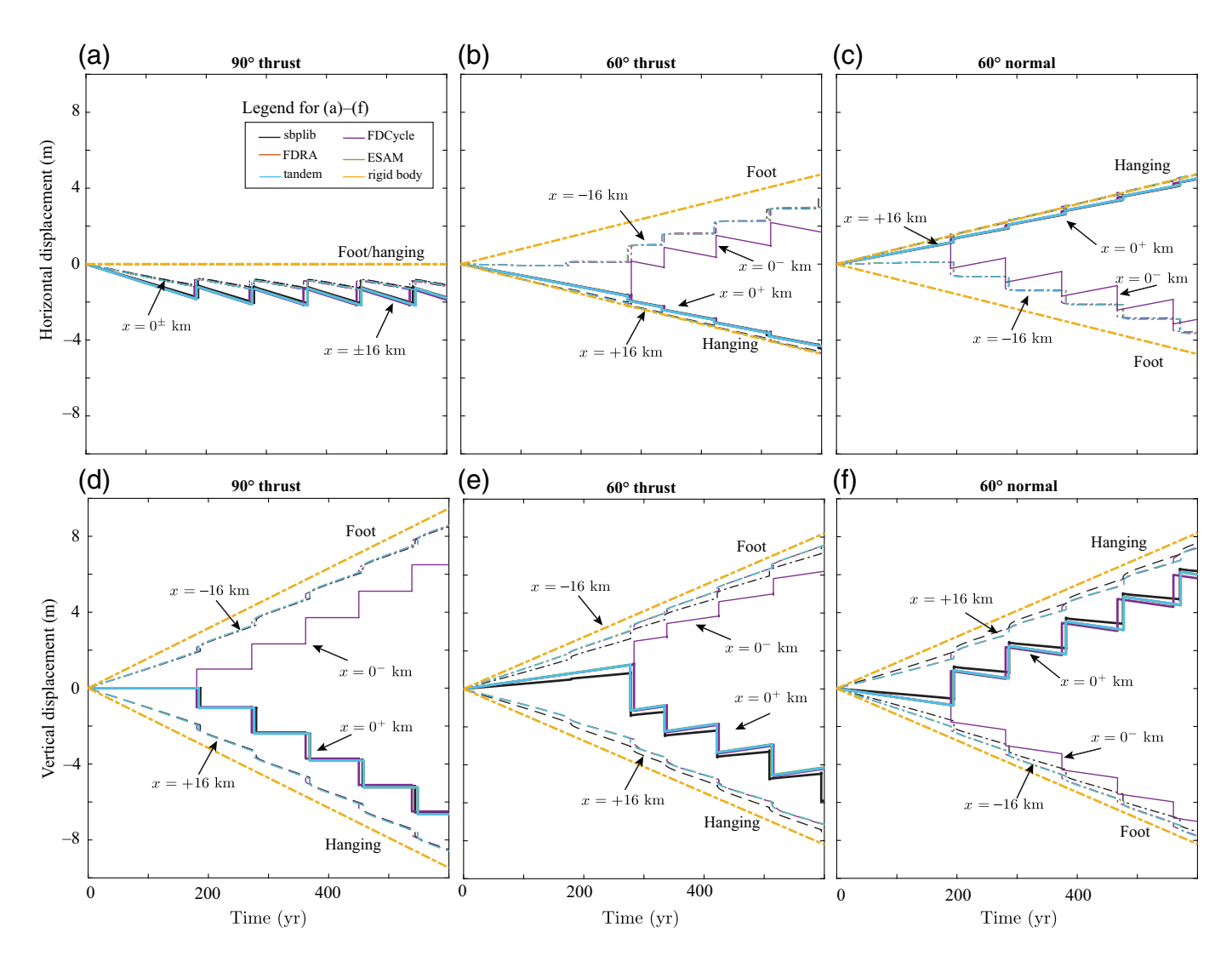


Figure 12. Horizontal and vertical components of surface displacement across a subset of codes at surface stations $x=0^+, x=\pm 16$ km for (a,d) 90° thrust, (b,e) 60° thrust, and (c,f) 60° normal. Also shown is surface station at $x=0^-$ (not solicited by benchmark description) from FDCycle

code for reference and the rigid body (far field) translation (in yellow) in which the text indicates motion on either the hanging or foot wall. The color version of this figure is available only in the electronic edition.

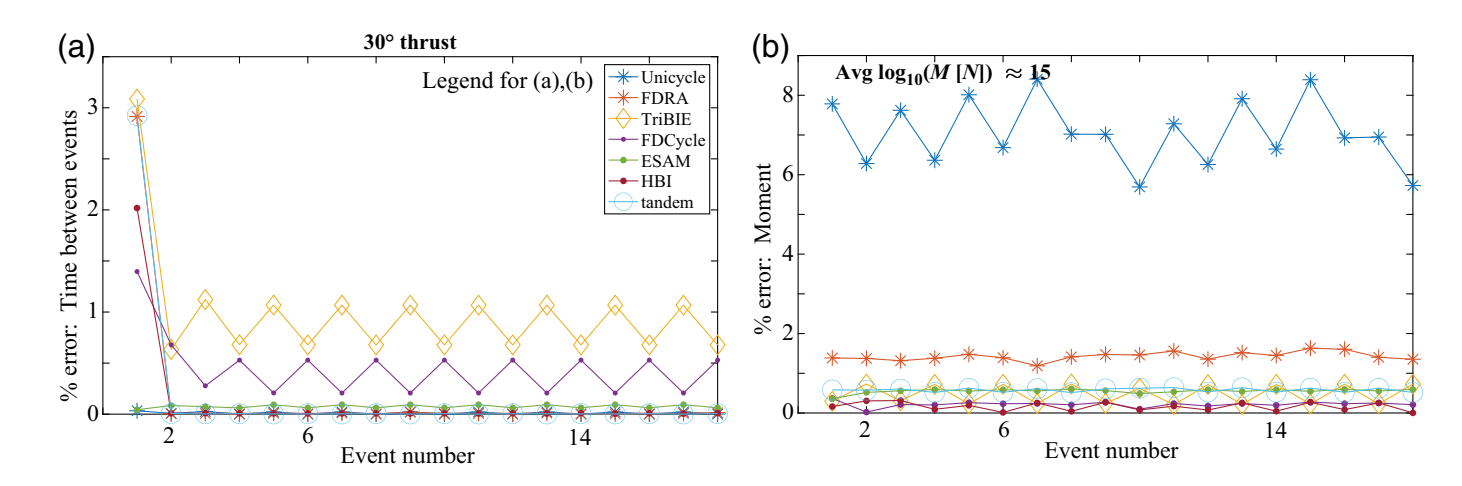
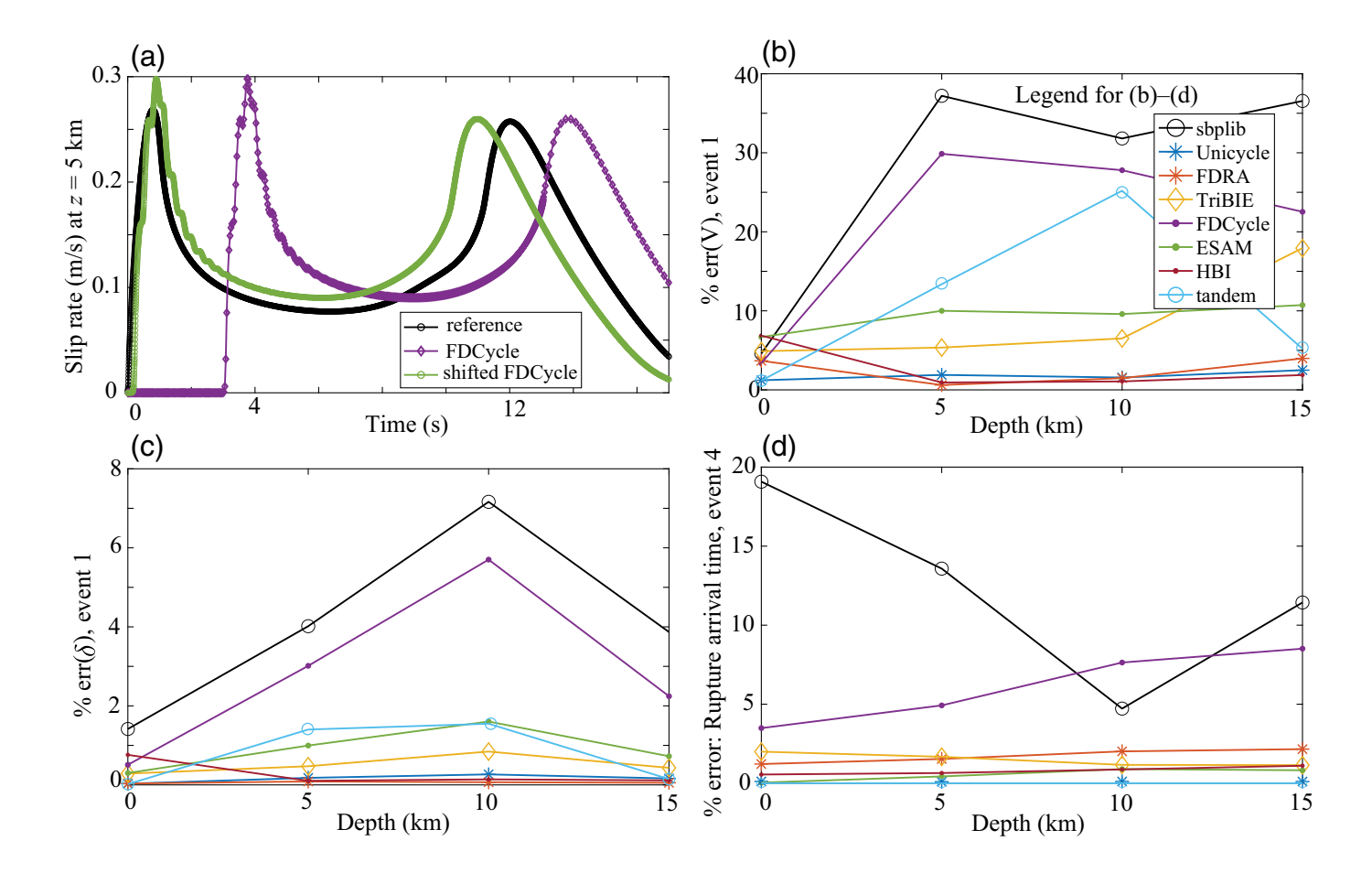


Figure 13. Long-term quantitative metric comparisons for BP3-QD (30° thrust fault scenario) show percent errors in (a) interevent times and (b) moment plotted against event number, in which error is relative to the

reference solution R_2 (with average magnitude $\log_{10}(M[N]) \approx 15$). The color version of this figure is available only in the electronic edition.

• Bulletin of the Seismological Society of America

www.bssaonline.org Volume 113 Number 2 April 2023



reference simulation). We increase L_x and L_z twofold (but maintain a cell size of 200 m to support computational feasibility), and these discrepancies are reduced up to a point: at least, single characteristic events emerge; however, the interevent times still differ by several years. Increasing the order of accuracy from p=4 to p=6 does not further reduce the discrepancy either. Figure 15b, however, shows that this discrepancy can be much further improved by also reducing the grid spacing from 200 to 100 m. This is further evidenced in the coseismic time series in Figure 15c in which much improvement is made with smaller grid spacing, but not markedly improved with higher p. The outliers noted previously we posit would benefit from both increased domain size and decreased cell size, if computationally feasible.

SUMMARY AND DISCUSSION

In this work, we find good agreements across participating numerical codes for both the benchmark problems. Here, we take "good" agreement to mean that many resolved features (over both short- and long-time scales) appear similar throughout the simulation period. We infer that numerical differences across codes are thus sufficiently small, such that the prominent features of these benchmark problems remain comparable (by visual inspection) throughout long-term earthquake sequences, that is, the numerical differences do not appear to substantially alter the behavior of the system, and we, therefore, believe that

Figure 14. Short-term quantitative metric comparisons for BP3-QD (30° thrust fault scenario) focus on a single coseismic event and shift all comparative time series to minimize errors, as illustrated in (a) for the FDCycle code. Percent errors against reference solution R_2 shown against depth in (b) slip rate and (c) slip during event 1, and for (d) rupture arrival time during event 4. The color version of this figure is available only in the electronic edition.

the resolved behavior in all the simulations is reliably representative of the physics.

To refine these assessments in a more quantitative manner, we develop both long- and short-term metrics, which enable us to explore sensitivity to computational domain size and grid spacing, as well as compute errors across model results against a well-resolved reference solution. For the SBEM-based reference solution for BP1-FD, we generally find larger errors for smaller domain size, with less sensitivity to the cell sizes considered, provided the cell sizes are small enough to resolve the important length scales in the problem, such as the cohesive zone and nucleation sizes. These results better inform our choices of these computational parameters, although we caution that exploratory studies are still needed to assess model sensitivity, given the wide range of numerical methods and parameters. Quantitative comparisons across participating codes in BP1-FD show excellent agreement in terms of long-term metrics, in which percent errors

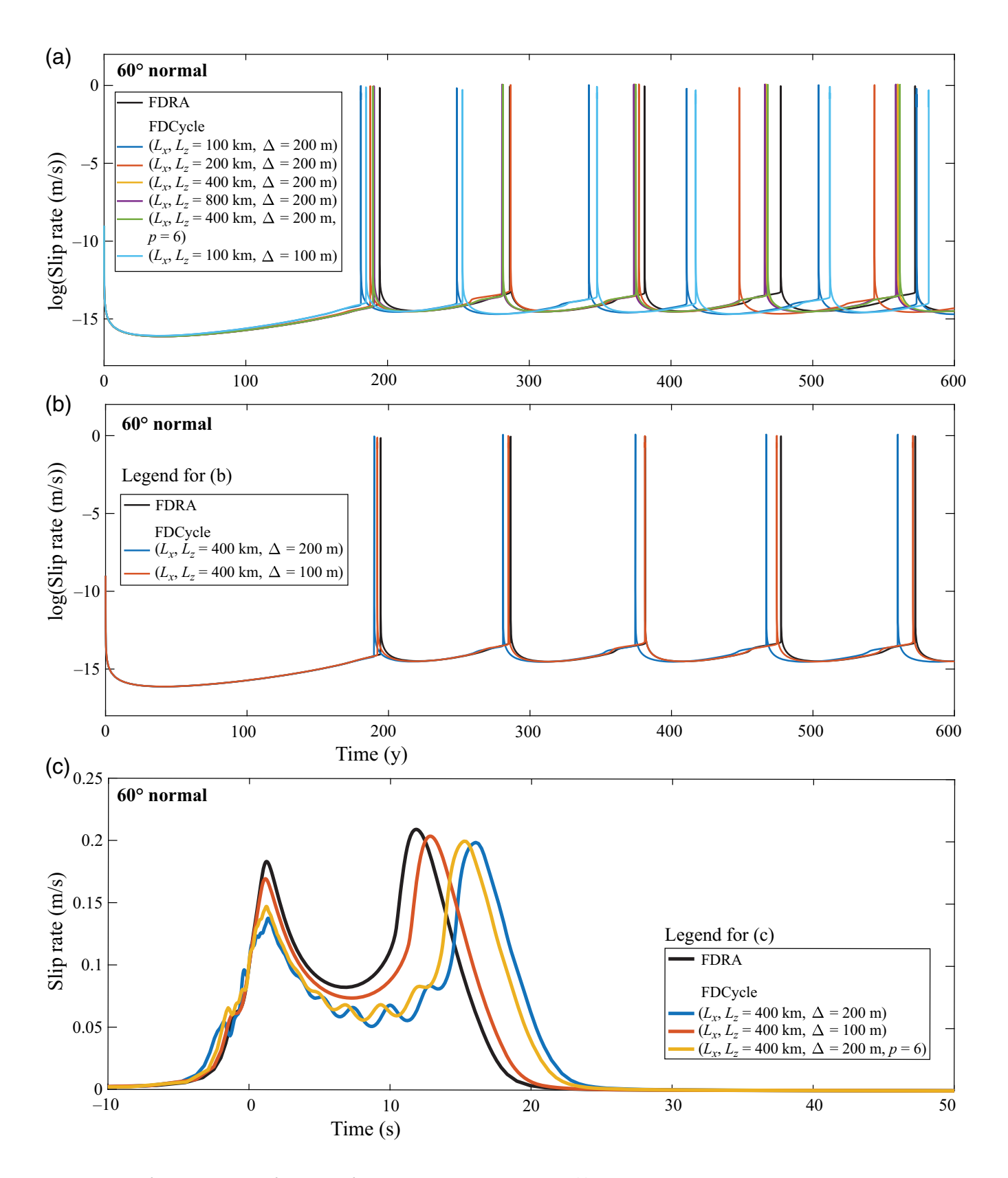


Figure 15. Results from the 60° normal-faulting case from FDCycle compared to FDRA code (used as a reference). (a) Long-term time series of slip rate for results from FDCycle with varying domain sizes, and different orders of accuracy and cell sizes. (b) Long-term time series results from a decreased

cell size. (c) Better agreement in coseismic time series is achieved with larger domain sizes and smaller grid spacing, whereas increasing the order of accuracy provides only nominal improvement. The color version of this figure is available only in the electronic edition.

are all well below 5%. Errors corresponding to short-term (coseismic) metrics are larger for integrated slip rates (between about 2% and 40%) but comparable with errors in peak slip rates reported in the dynamic rupture scenarios of Day *et al.* (2005). Errors in integrated slip are only a few percent at the most, whereas errors in rupture arrival time are all at or well below 10%.

For BP3-QD, we find good agreements across codes for both thrust and normal faulting, and all dip angles are considered, except for a few outliers for which discrepancies we attribute to finite computational domain size effects: we demonstrate that we can obtain better matching results of long-term time series by increasing the computational domain size, with some further improvements to short-term, coseismic times series afforded by a decrease in cell size.

Quantitative comparisons across participating codes in BP3-QD again show excellent agreement in terms of long-term metrics, in which percent errors are all well below 10%. As in BP1-FD, errors corresponding to short-term (coseismic) metrics are larger for integrated slip rates (between about 2% and 40%), whereas errors in integrated slip are less than 10% and in rupture arrival time all at or well below 10% (when disregarding the outliers noted).

The quantitative agreements obtained suggest that the problem formulations and numerical parameter choices (cell size and domain size) made by participating codes appear sufficient in obtaining well-matching results. The metrics defined in this work, along with those in Jiang et al. (2022), constitute initial steps toward quantitatively assessing SEAS model outcomes. One of our goals for future exercises is to improve and develop metrics that target different features of earthquake source processes, including errors in off-fault time series and statistical properties of earthquake sequences. Furthermore, these initial steps will help refine the descriptions of future benchmark descriptions and solicited model output (for example, we may need to request specific, highly sampled data to define more robust metrics).

In addition to obtaining good agreements across codes, in this work, we highlight some of the differences that the added features of full elastodynamics and geometric complexity (dipping faults) have on SEAS model outcomes. BP1-FD enables our first study of numerical considerations for fully dynamic SEAS simulations across a range of codes and computational frameworks. Although these simulations need to resolve key physical length scales, computational domain size is a persistent important parameter to obtain matching results. The criteria used by the volume-based codes to switch between methods for the quasi-static and dynamic periods vary across codes, and sufficient conditions to obtain matching results is reported. Good agreements across codes are obtained, in terms of number of characteristic events and recurrence times, as well as short-term processes (maximum slip rates, stress drops, and rupture speeds). We also compare model response to the quasidynamic simulations of BP1-QD. Although, in both the scenarios, characteristic events emerge, the simulations of BP1-FD are accompanied by higher slip rates and ruptures speeds, as well as more coseismic slip during dynamic events and longer interevent times compared to BP1-QD, underscoring the important effects of wave-mediated stress transfers.

In terms of model outcomes, the dipping fault geometries and sense of motion (thrust vs. normal) yield event sequences ranging from one to four distinct characteristic events (with different interevent times and magnitudes) within a simulation. The comparison of off-fault surface displacements revealed a problem statement ambiguity in the assumed remote boundary conditions, which, once clearly specified, enabled us to obtain good agreements across the codes. The simulations reveal notable asymmetry in ground motion on the hanging and foot walls, which would have implications for seismic hazard.

BP1-FD and BP3-QD constitute important first steps toward verifying SEAS codes with increased physical and geometric complexities. The ability to explore numerical considerations across a wide variety of codes is invaluable for the advancement of SEAS codes, especially when dependencies on numerical factors (such as the switching criterion used in several volumebased codes for BP1-FD) can be more deeply explored through community efforts, enabling the sharing of successful strategies. In addition, spatial resolution and domain size are computationally costly to explore individually and also benefit from community efforts. However, the associated computational costs will continue to increase with new physical and geometric features, particularly, as we move to 3D simulations. Currently, the majority of the volume-based codes involve serial implementations that may inhibit their ability to participate in the future benchmarks, unless length scales are chosen carefully to make computations tractable. High-performance computing (HPC) techniques for the volume-based codes will be necessary for future SEAS simulations, considering a wider ranges of length scales (requiring higher resolution), and/or 3D simulations.

We expect that future SEAS simulations will regularly include full elastodynamic effects and nonplanar fault geometries, which are known to influence earthquake recurrence times, magnitudes, strong ground shaking, and ground-motion asymmetry, all of which have important implications for assessment of seismic hazard. We expect to be able to leverage many of the important findings of the Southern California Earthquake Center (SCEC)/U.S. Geological Survey Spontaneous Rupture Code Verification project (Harris et al., 2009, 2018; Barall and Harris, 2014), not only in advancing SEAS simulations with similar HPC techniques but also in defining benchmark problems with advanced physical and geometric features (e.g., plasticity and rough faults). An important goal of our SEAS exercises is to also develop insight into appropriate, self-consistent initial conditions prior to rupture that can then inform detailed dynamic rupture simulations. Finally, our future SEAS simulations will aim to consider larger-scale fault systems, including geometrically complex fault networks, and assess the importance of different physical ingredients, such as full inertial effects, for physics-based models of seismic hazard.

DATA AND RESOURCES

Our online platform (https://strike.scec.org/cvws/seas/, last accessed December 2022) is being developed and maintained by Michael Barall. The data for local fault and surface properties are stored on the platform. The supplemental material includes complete problem descriptions for BP1-FD and BP3-FD, self-convergence studies of codes used to obtain the reference solutions, and additional figures for BP3-QD simulations. Author Contributions: Brittany A. Erickson and Junle Jiang designed the benchmark problems and organized the workshops. Brittany A. Erickson analyzed results and led the writing of the article with significant input from Junle Jiang and Valère Lambert; Valère Lambert and Sylvian D. Barbot provided data for convergence tests; remaining authors are listed alphabetically. All authors provided feedback on benchmark design, participated in the benchmark exercises, and helped revise the article.

DECLARATION OF COMPETING INTERESTS

The authors acknowledge that there are no conflicts of interest recorded.

ACKNOWLEDGMENTS

This article benefitted from constructive feedback provided by Pierre Dublanchet, a second anonymous reviewer, and the associate editor at BSSA. Thanks to Michael Barall who developed and maintains the online platform, and to Ruth Harris for mentorship in leading group code verification exercises. Brittany A. Erickson and Junle Jiang were supported through the Southern California Earthquake Center, Grant Number 18099, 19109, 20113, and 21065. The simulations with BICyclE (J. J.) were conducted with the Award Number EAR170014 from the Extreme Science and Engineering Discovery Environment (XSEDE), which is supported by U.S. National Science Foundation (NSF) Grant Number ACI-1548562. Junle Jiang was supported in part by the NSF Award Number EAR-2221569. The simulations with BICyclE (Valère Lambert and Nadia Lapusta) were carried out on the High-Performance Computing Center cluster of the California Institute of Technology with the grant support from Southern California Earthquake Center (SCEC). Sylvian D Barbot was supported in part by the NSF Award Number EAR-1848192. Valère Lambert was supported by an NSF Postdoctoral Fellowship. L. D. Z. was supported by the European Research Council (ERC) Synergy Grant FEAR (ID: 856559). Jean-Paul Ampuero and Chao Liang were supported by the French National Research Agency through the UCAJEDI Investments in the Future Project Number ANR-15-IDEX-01. Tobias W. Harvey and Alexandre Chen were supported by NSF Award Number EAR-1916992 and simulations benefited from access to the University of Oregon high performance computing cluster, Talapas. Duo Li, Casper Pranger, Carsten Uphoff, and Alice-Agnes Gabriel were supported by ERC StG TEAR, Grant Number 852992 and in part by NSF Award Number EAR-2121666. The simulations with HBI are supported in part by Japan Society for the Promotion of Science (JSPS) KAKENHI Grant Numbers 19J21676 and 19K04031. Meng Li, Casper Pranger, and Ylona van Dinther were supported by Council (NWO) Dutch Research Grant DEEP.NL.2018.037, Swiss National Science Foundation (SNSF) Grant Number 200021169880, and EU-MC ITN Grant Number 604713. Ahmed E. Elbanna and Mohamed Abdelmeguid acknowledge support from NSF CAREER Award Number 1753249 and the DOE under Award Number DE-FE0031685. Prithvi Thakur and Yihe Huang were supported by NSF Award Number EAR-1943742. Yoshihiro Kaneko was supported by JSPS KAKENHI Grant Number 21H05206. Martin Almquist was supported by the Knut and Alice Wallenberg Foundation (Dnr. KAW 2016.0498). Yajing Liu was supported by the Natural Sciences and Engineering Research Council of Canada (NSERC) Discovery Grant Number RGPIN-2018-05389. Simulations of Earthquake Sequences and Aseismic Slip (SEAS)-themed workshops were funded by SCEC Award Numbers 17151, 18102, 19110, 20120, and 21139. SCEC is funded by NSF Cooperative Agreement NumbersEAR-0529922 and U.S. Geological Survey (USGS) Cooperative Agreement Number 07HQAG0008. This is a SCEC Contribution Number 12627.

REFERENCES

- Abdelmeguid, M., X. Ma, and A. Elbanna (2019). A novel hybrid finite element-spectral boundary integral scheme for modeling earth-quake cycles: Application to rate and state faults with low-velocity zones, *J. Geophys. Res.* **124**, no. 12, 12,854–12,881, doi: 10.1029/2019jb018036.
- Allison, K., and E. M. Dunham (2018). Earthquake cycle simulations with rate-and-state friction and power-law viscoelasticity, *Tectonophysics* **733**, 232–256, doi: 10.1016/j.tecto.2017.10.021.
- Ampuero, J.-P., and A. M. Rubin (2008). Earthquake nucleation on rate and state faults—Aging and slip laws, *J. Geophys. Res.* **113**, no. B1, 1–21, doi: 10.1029/2007JB005082.
- Andrews, D. J. (1976a). Rupture velocity of plane strain shear cracks, *J. Geophys. Res.* **81**, no. 32, 5679–5687.
- Andrews, D. J. (1976b). Rupture propagation with finite stress in antiplane strain, *J. Geophys. Res.* **81**, 3575–3582.
- Andrews, D. J. (1976c). Rupture velocity of plane strain shear cracks, *J. Geophys. Res.* **81**, 5679–5687.
- Ariyoshi, K., T. Matsuzawa, J.-P. Ampuero, R. Nakata, T. Hori, Y. Kaneda, R. Hino, and A. Hasegawa (2012). Migration process of very low-frequency events based on a chain-reaction model and its application to the detection of preseismic slip for megathrust earthquakes, *Earth Planets Space* **64**, no. 8, 693–702, doi: 10.5047/eps.2010.09.003.
- Barall, M., and R. A. Harris (2014). Metrics for comparing dynamic earthquake rupture simulations, *Seismol. Res. Lett.* **86,** no. 1, 223–235, doi: 10.1785/0220140122.
- Barbot, S. (2019). Slow-slip, slow earthquakes, period-two cycles, full and partial ruptures, and deterministic chaos in a single asperity fault, *Tectonophysics* doi: 10.1016/j.tecto.2019.228171.
- Barbot, S. (2021). A spectral boundary-integral method for quasi-dynamic ruptures of multiple parallel faults, *Bull. Seismol. Soc. Am.* **111**, no. 3, 1614–1630, doi: 10.1785/0120210004.
- Barbot, S., N. Lapusta, and J.-P. Avouac (2012). Under the hood of the earthquake machine: Toward predictive modeling of the seismic cycle, *Science* **336**, no. 6082, 707–710, doi: 10.1126/science.1218796.

- Bradley, A. M. (2014). Software for efficient static dislocation–traction calculations in fault simulators, *Seismol. Res. Lett.* **85**, no. 6, 1358–1365, doi: 10.1785/0220140092.
- Cattania, C. (2019). Complex earthquake behavior on simple faults, *Geophys. Res. Lett.* doi: 10.31223/osf.io/hgbjx.
- Dal Zilio, L., N. Lapusta, J.-P. Avouac, and T. Gerya (2021). Subduction earthquake sequences in a non-linear visco-elastoplastic megathrust, *Geophys. J. Int.* 229, no. 2, 1098–1121, doi: 10.1093/gji/ggab521.
- Day, S. M., L. A. Dalguer, N. Lapusta, and Y. Liu (2005). Comparison of finite difference and boundary integral solutions to three-dimensional spontaneous rupture, *J. Geophys. Res.* **110**, no. B12, doi: 10.1029/2005JB003813.
- Dieterich, J. H. (1979). Modeling of rock friction: 1. Experimental results and constitutive equations, *J. Geophys. Res.* **84**, no. B5, 2161–2168, doi: 10.1029/JB084iB05p02161.
- Dieterich, J. H. (1992). Earthquake nucleation on faults with rate- and state-dependent strength, *Tectonophysics* **211**, 115–134.
- Dieterich, J. H., and K. B. Richards-Dinger (2010). Earthquake recurrence in simulated fault systems, *Pure Appl. Geophys.* **167**, no. 8, 1087–1104, doi: 10.1007/s00024-010-0094-0.
- Duan, B., and D. D. Oglesby (2005). The dynamics of thrust and normal faults over multiple earthquake cycles: Effects of dipping fault geometry, *Bull. Seismol. Soc. Am.* 95, no. 5, 1623–1636, doi: 10.1785/0120040234.
- Dublanchet, P. (2022). Seismicity modulation in a 3-D rate-and-state interacting fault population model, *Geophys. J. Int.* **229**, no. 3, 1804–1823, doi: 10.1093/gji/ggac023.
- Dunham, E. M., D. Belanger, L. Cong, and J. E. Kozdon (2011). Earthquake ruptures with strongly rate-weakening friction and off-fault plasticity, part 1: Planar faults, *Bull. Seismol. Soc. Am.* **101**, no. 5, 2296–2307, doi: 10.1785/0120100075.
- Dunyu, L., B. Duan, and B. Luo (2020). EQsimu: A 3-D finite element dynamic earthquake simulator for multicycle dynamics of geometrically complex faults governed by rate- and state-dependent friction, *Geophys. J. Int.* **220**, 598–609, doi: 10.1093/gii/ggz475.
- Duru, K., K. L. Allison, M. Rivet, and E. M. Dunham (2019). Dynamic rupture and earthquake sequence simulations using the wave equation in second-order form, *Geophys. J. Int.* 219, no. 2, 796–815, doi: 10.1093/gji/ggz319.
- Erickson, B. A., and E. M. Dunham (2014). An efficient numerical method for earthquake cycles in heterogeneous media: Alternating subbasin and surface-rupturing events on faults crossing a sedimentary basin, *J. Geophys. Res.* 119, no. 4, 3290–3316, doi: 10.1002/ 2013JB010614.
- Erickson, B. A., E. M. Dunham, and A. Khosravifar (2017). A finite difference method for off-fault plasticity throughout the earthquake cycle, *J. Mech. Phys. Solids* **109**, 50–77, doi: 10.1016/j.jmps.2017.08.002.
- Erickson, B. A., J. E. Kozdon, and T. Harvey (2022). A non-stiff summation-by-parts finite difference method for the scalar wave equation in second order form: Characteristic boundary conditions and nonlinear interfaces, *J. Sci. Comput.* **93**, no. 1, 17, doi: 10.1007/s10915-022-01961-1.
- Erickson, B. A., J. Jiang, M. Barall, N. Lapusta, E. M. Dunham, R. Harris, L. S. Abrahams, K. L. Allison, J. P. Ampuero, S. Barbot, et al. (2020). The community code verification exercise for simulating sequences of earthquakes and aseismic slip (SEAS), Seismol. Res. Lett. 91, 874–890, doi: 10.1785/0220190248.

- Hajarolasvadi, S., and A. E. Elbanna (2017). A new hybrid numerical scheme for modelling elastodynamics in unbounded media with near-source heterogeneities, *Geophys. J. Int.* **211**, no. 2, 851–864, doi: 10.1093/gji/ggx337.
- Harris, R. A., and S. M. Day (1993). Dynamics of fault interaction: Parallel strike-slip faults, *J. Geophys. Res.* **98**, no. B3, 4461–4472, doi: 10.1029/92JB02272.
- Harris, R. A., M. Barall, R. Archuleta, E. Dunham, B. Aagaard, J. P. Ampuero, H. Bhat, V. Cruz-Atienza, L. Dalguer, P. Dawson, et al. (2009). The SCEC/USGS dynamic earthquake rupture code verification exercise, Seismol. Res. Lett. 80, 119–126, doi: 10.1785/gssrl.80.1.119.
- Harris, R. A., M. Barall, B. Aagaard, S. Ma, D. Roten, K. Olsen, B. Duan, D. Liu, B. Luo, K. Bai, *et al.* (2018). A suite of exercises for verifying dynamic earthquake rupture codes, *Seismol. Res. Lett.* **89**, no. 3, 1146–1162, doi: 10.1785/0220170222.
- Harvey, T. W., B. A. Erickson, and J. Kozdon (2022). A high-order accurate summation-by-parts finite difference method for fullydynamic earthquake sequence simulations within sedimentary basins, J. Geophys. Res. doi: 10.31223/X58K95.
- Jiang, J., and N. Lapusta (2017). Connecting depth limits of interseismic locking, microseismicity, and large earthquakes in models of long-term fault slip, *J. Geophys. Res.* 122, no. 8, 6491–6523, doi: 10.1002/2017JB014030.
- Jiang, J., B. A. Erickson, V. R. Lambert, J. P. Ampuero, R. Ando, S. D. Barbot, C. Cattania, L. D. Zilio, B. Duan, E. M. Dunham, et al. (2022). Community-driven code comparisons for three-dimensional dynamic modeling of sequences of earthquakes and aseismic slip, J. Geophys. Res. 127, no. 3, e2021JB023519, doi: 10.1029/2021JB023519.
- Kaneko, Y., J.-P. Ampuero, and N. Lapusta (2011). Spectral-element simulations of long-term fault slip: Effect of low-rigidity layers on earthquake-cycle dynamics, *J. Geophys. Res.* **116**, no. B10, 1–18, doi: 10.1029/2011JB008395.
- Kozdon, J., B. A. Erickson, and L. C. Wilcox (2020). Hybridized summation-by-parts finite difference methods, *J. Sci. Comput.* **87**, no. 85, 1–28, doi: 10.1007/s10915-021-01448-5.
- Lambert, V., and S. Barbot (2016). Contribution of viscoelastic flow in earthquake cycles within the lithosphere-asthenosphere system, *Geophys. Res. Lett.* **43**, no. 19, 142–154.
- Lambert, V., and N. Lapusta (2021). Resolving simulated sequences of earthquakes and fault interactions: Implications for physics-based seismic hazard assessment, *J. Geophys. Res.* 126, no. 10, e2021JB022193, doi: 10.1029/2021JB022193.
- Lapusta, N., and Y. Liu (2009). Three-dimensional boundary integral modeling of spontaneous earthquake sequences and aseismic slip, *J. Geophys. Res.* **114**, no. B9, 1–25, doi: 10.1029/2008JB005934.
- Lapusta, N., and J. R. Rice (2003). Nucleation and early seismic propagation of small and large events in a crustal earthquake model, *J. Geophys. Res.* **108**, no. B4, 1–18.
- Lapusta, N., J. R. Rice, Y. Ben-Zion, and G. Zheng (2000). Elastodynamic analysis for slow tectonic loading with spontaneous rupture episodes on faults with rate- and state-dependent friction, *J. Geophys. Res.* **105**, no. B10, 23,765–23,789, doi: 10.1029/2000JB900250.
- Li, D., and Y. Liu (2016). Spatiotemporal evolution of slow slip events in a nonplanar fault model for northern Cascadia subduction zone, *J. Geophys. Res.* 121, no. 9, 6828–6845, doi: 10.1002/2016jb012857.

- Li, D., and Y. Liu (2017). Modeling slow-slip segmentation in Cascadia subduction zone constrained by tremor locations and gravity anomalies, *J. Geophys. Res.* 122, 3138–3157, doi: 10.1002/2016JB013778.
- Li, M., C. Pranger, and Y. van Dinther (2022). Characteristics of earth-quake cycles: A cross-dimensional comparison of 0D to 3D numerical models, *J. Geophys. Res.* **127**, no. 8, e2021JB023726, doi: 10.1029/2021JB023726.
- Liu, Y., and N. Lapusta (2008). Transition of mode ii cracks from sub-Rayleigh to intersonic speeds in the presence of favorable heterogeneity, *J. Mech. Phys. Solids* **56**, no. 1, 25–50, doi: 10.1016/j.jmps.2007.06.005.
- Liu, Y., and J. R. Rice (2007). Spontaneous and triggered aseismic deformation transients in a subduction fault model, *J. Geophys. Res.* **112**, no. B9, 1–23, doi: 10.1029/2007JB004930.
- Ma, S., and G. Beroza (2008). Rupture dynamics on a bimaterial interface for dipping faults, *Bull. Seismol. Soc. Am.* **98,** 1642–1658, doi: 10.1785/0120070201.
- Marone, C. (1998). Laboratory-derived friction laws and their application to seismic faulting, *Annu. Rev. Earth Planet. Sci.* **26,** no. 1, 643–696, doi: 10.1146/annurev.earth.26.1.643.
- Ozawa, S., and R. Ando (2021). Mainshock and aftershock sequence simulation in geometrically complex fault zones, *J. Geophys. Res.* **126**, no. 2, e2020JB020865, doi: 10.1029/2020JB020865.
- Palmer, A. C., and J. R. Rice (1973). The growth of slip surfaces in the progressive failure of over-consolidated clay, *Proc. Math. Phys. Sci.* **332**, no. 1591, 527–548, doi: 10.1098/rspa.1973.0040.
- Perfettini, H., and J.-P. Ampuero (2008). Dynamics of a velocity strengthening fault region: Implications for slow earthquakes and postseismic slip, *J. Geophys. Res.* **113**, no. B9, 1–22, doi: 10.1029/2007JB005398.
- Pranger, C. (2020). Unstable physical processes operating on self-governing fault systems, improved modeling methodology, *Ph.D. Thesis*, ETH Zurich.
- Preuss, S., R. Herrendörfer, T. Gerya, J.-P. Ampuero, and Y. van Dinther (2019). Seismic and aseismic fault growth lead to different fault orientations, *J. Geophys. Res.* 124, no. 8, 8867–8889, doi: 10.1029/2019JB017324.
- Rice, J. R. (1993). Spatio-temporal complexity of slip on a fault, *J. Geophys. Res.* **98**, no. B6, 9885–9907.
- Rice, J. R., and A. L. Ruina (1983). Stability of steady frictional slipping, J. Appl. Mech. 50, 343–349.
- Richards-Dinger, K., and J. H. Dieterich (2012). RSQSim earthquake simulator, *Bull. Seismol. Soc. Am.* **83**, no. 6, 983–990, doi: 10.1785/0220120105.
- Romanet, P., and S. Ozawa (2021). Fully dynamic earthquake cycle simulations on a nonplanar fault using the spectral boundary integral element method (sBIEM), *Bull. Seismol. Soc. Am.* **112,** no. 1, 78–97, doi: 10.1785/0120210178.
- Rubin, A. M., and J.-P. Ampuero (2005). Earthquake nucleation on (aging) rate and state faults, *J. Geophys. Res.* **110**, no. B11, 1–24, doi: 10.1029/2005JB003686.
- Ruina, A. (1983). Slip instability and state variable friction laws, J. Geophys. Res. 88, no. B12, 10,359–10,370, doi: 10.1029/ JB088iB12p10359.
- Rundle, P. B., J. Rundle, K. Tiampo, A. Donnellan, and D. Turcotte (2006). Virtual California: Fault model, frictional parameters, applications, in *Computational Earthquake Physics: Simulations, Analysis*

- and Infrastructure, Part I, X.-C. Yin, P. Mora, A. Donnellan, and M. Matsu'ura (Editors), 1819–1846, Birkhäuser Basel, Basel.
- Segall, P., and A. M. Bradley (2012). Slow-slip evolves into megathrust earthquakes in 2D numerical simulations, *Geophys. Res. Lett.* 39, no. 18, 1–5, doi: 10.1029/2012GL052811.
- Shi, P., M. Wei, and S. Barbot (2022). Contribution of viscoelastic stress to the synchronization of earthquake cycles on oceanic transform faults, *J. Geophys. Res.* **127**, no. 8, e2022JB024069, doi: 10.1029/2022JB024069.
- Shi, Z., and S. M. Day (2013). Rupture dynamics and ground motion from 3-D rough-fault simulations, *J. Geophys. Res.* **118**, 1–20, doi: 10.1002/jgrb.50094.
- Thomas, M. Y., N. Lapusta, H. Noda, and J.-P. Avouac (2014). Quasi-dynamic versus fully dynamic simulations of earthquakes and aseismic slip with and without enhanced coseismic weakening, *J. Geophys. Res.* **119**, 1986–2004.
- Tse, S. T., and J. R. Rice (1986). Crustal earthquake instability in relation to the depth variation of frictional slip properties, *J. Geophys. Res.* **91**, no. B9, 9452–9472.
- Tullis, T. E., K. Richards-Dinger, M. Barall, J. H. Dieterich, E. H. Field, E. M. Heien, L. H. Kellogg, F. F. Pollitz, J. B. Rundle, M. K. Sachs, et al. (2012a). Generic earthquake simulator, Seismol. Res. Lett. 83, 959–963, doi: 10.1785/0220120093.
- Tullis, T. E., K. B. Richards-Dinger, M. Barall, J. H. Dieterich, E. H. Field, E. M. Heien, L. Kellogg, F. F. Pollitz, J. B. Rundle, M. K. Sachs, et al. (2012b). Comparison among observations and earth-quake simulator results for the allcal2 California fault model, Seismol. Res. Lett. 83, 994–1006.
- Uenishi, K., and J. R. Rice (2003). Universal nucleation length for slip-weakening rupture instability under nonuniform fault loading, J. Geophys. Res. 108, no. B1, 1–14, doi: 10.1029/2001JB001681.
- Uphoff, C., D. A. May, and A.-A. Gabriel (2022). Preprint: A discontinuous Galerkin method for sequences of earthquakes and aseismic slip on multiple faults using unstructured curvilinear grids, doi: 10.31223/X50627.
- Ward, S. N. (2012). ALLCAL earthquake simulator, Seismol. Res. Lett. 83, no. 6, 964–972, doi: 10.1785/0220120056.

AUTHORS AND AFFILIATIONS

Brittany A. Erickson: Department of Computer Science, Department of Earth Science, University of Oregon, Eugene, Oregon, U.S.A., https://orcid.org/0000-0001-9457-8572; Junle Jiang: School of Geosciences, University of Oklahoma, Norman, Oklahoma, U.S.A., https://orcid.org/0000-0002-8796-5846; Valère Lambert: Department of Earth and Planetary Sciences, University of California, Santa Cruz, California, U.S.A., https://orcid.org/0000-0002-6174-9651; Sylvain D. Barbot: Earth Science Department, University of Southern California, Los Angeles, California, U.S.A., Dhttps:// orcid.org/0000-0003-4257-7409; Mohamed Abdelmeguid: Department of Civil and Environmental Engineering, University of Illinois at Urbana Champaign, Urbana, Illinois, U.S.A., https:// orcid.org/0000-0002-3985-1721; Martin Almquist: Department of Information Technology, Division of Scientific Computing, Uppsala University, Uppsala, Sweden, https://orcid.org/0000-0002-8012-5860; Jean-Paul Ampuero: Géoazur Laboratory, Université Côte d'Azur, IRD, CNRS, Observatoire de la Côte d'Azur, Valbonne,

France, https://orcid.org/0000-0002-4827-7987; Ryosuke Ando: Department of Earth and Planetary Science, The University of Tokyo, Tokyo, Japan, https://orcid.org/0000-0002-6205-3699; Camilla Cattania: Department of Earth, Atmospheric, and Planetary Sciences, Massachusetts Institute of Technology, Cambridge, Massachusetts, U.S.A., https://orcid.org/0000-0003-0031-1696; Alexandre Chen: Department of Computer Science, Department of Earth Science, University of Oregon, Eugene, Oregon, U.S.A.; Luca Dal Zilio: Department of Earth Sciences, Institute of Geophysics, ETH Zurich, Zurich, Switzerland, https://orcid.org/ 0000-0002-5642-0894; Shuai Deng: Institute for Disaster Management and Reconstruction (IDMR), Sichuan University, Chengdu, China; Eric M. Dunham: Department of Geophysics, Institute for Computational and Mathematical Engineering, Stanford University, Stanford, California, U.S.A., https://orcid.org/0000-0003-0804-7746; Ahmed E. Elbanna: Department of Civil and Environmental Engineering, Beckman Institute of Advanced Science and Technology, Urbana, Illinois, U.S.A.; Alice-Agnes Gabriel: Scripps Institution of Oceanography, UC San Diego, La Jolla, California, U.S.A.; Department of Earth and Environmental Sciences, University of Michigan, Ann Arbor, Michigan, U.S.A., 6 https:// orcid.org/0000-0003-0112-8412; Tobias W. Harvey: Department of Computer Science, Department of Earth Science, University of Oregon, Eugene, Oregon, U.S.A.; Yihe Huang: Department of Earth and Environmental Sciences, University of Michigan, Ann Arbor, Michigan, U.S.A., https://orcid.org/0000-0001-5270-9378; Yoshihiro Kaneko: Department of Geophysics, Graduate School of Science, Kyoto University, Kyoto, Japan, https://orcid.org/0000-0003-2342-0131; Jeremy E. Kozdon: Department of Applied Mathematics, Naval Postgraduate School, Monterey, California, U.S.A.; HPC Applications Engineer at NextSilicon, Giv'atayim, Israel, https://orcid.org/0000-0002-2493-4292; Nadia Lapusta: Department of Mechanical and Civil Engineering and Seismological Laboratory, California Institute of Technology, Pasadena, California, U.S.A., https://orcid.org/0000-0001-6558-0323; Duo Li:

Department of Earth and Environmental Sciences, Ludwig-Maximilians-University, Munich, Germany, https://orcid.org/0000-0002-8641-337X; Meng Li: Department of Earth Sciences, Utrecht University, Utrecht, Netherlands, https://orcid.org/0000-0001-9459-7167; Chao Liang: Institute for Disaster Management and Reconstruction (IDMR), Sichuan University, Chengdu, China, https://orcid.org/0000-0001-5237-9655; Yajing Liu: Department of Earth and Planetary Sciences, McGill University, Montréal, Québec, Canada, https://orcid.org/0000-0002-5323-8077; So Ozawa: Department of Earth and Planetary Science, The University of Tokyo, Tokyo, Japan, https://orcid.org/0000-0002-6507-6925; Andrea Perez-Silva: School of Geography, Environment and Earth Sciences, Victoria University of Wellington, Wellington, New Zealand, https://orcid.org/0000-0002-8555-5122; Casper Pranger: Department of Earth and Environmental Sciences, Ludwig-Maximilians-University, Munich, Germany, https://orcid.org/0000-0002-8943-896X; Paul Segall: Geophysics Department, Stanford University, Stanford, California, U.S.A., https://orcid.org/0000-0001-5973-471X; Yudong Sun: Department of Earth, Atmospheric, and Planetary Sciences, Massachusetts Institute of Technology, Cambridge, Massachusetts, U.S.A., https://orcid.org/0000-0003-0809-936X; Prithvi Thakur: Department of Earth and Environmental Sciences, University of Michigan, Ann Arbor, Michigan, U.S.A., https://orcid.org/0000-0001-6687-0787; Carsten Uphoff: Department of Earth and Environmental Sciences, Ludwig-Maximilians-University, Munich, Germany, https://orcid.org/0000-0002-9169-7485; Ylona van Dinther: Department of Earth Sciences, Utrecht University, Utrecht, Netherlands, https://orcid.org/0000-0002-4273-8287; and Yuyun Yang: Department of Geophysics, Institute for Computational and Mathematical Engineering, Stanford University, Stanford, California, U.S.A., https://orcid.org/0000-0001-5260-8593

> Manuscript received 25 April 2022 Published online 10 January 2023